Numerical studies of rotationally controlled lock exchange flow over a sill

Magdeli Holmøy Asplin
Department of Mathematics
University of Bergen

May 28, 2018

Contents

1 Introduction

Long channels with steep sides that contains one or more submarine sills, defining one or more deep inner basins of the channel, are often referred to as fjords. The circulation in fjords is a complex composition of the contributions made from these characteristics (Farmer and Freeland, 1983).

River runoffs close to the head of the fjord supply the fjord with freshwater, while also possibly providing a current outwards in the surface layer. Due to melting snow in the mountains, there can be large seasonal variances in the runoff. It can also be affected by weather changes, mainly due to differences in precipitation, where more rain leads to more river runoff.

When entering the fjord, the freshwater meets the salt oceanic water, mixing processes begin, and the result is a brackish layer at the surface. This layer differs vastly in thickness due to the variances in the river runoff, with a thicker and more extensive layer at high runoff, and a thinner and less extended arm of brackish water at times of low runoff. In extreme cases, the runoff can lead to blocking, meaning no outside water are able to enter the fjord because of high velocities outwards. This is when the brackish layer reaches all the way down to sill level, or even below.

Underneath there is an intermediate layer, typically from 50-100 m depth, or the sill depth if shallower, and up to the surface or the bottom of the brackish layer (Stigebrandt, 2012). The intermediate layer is a result of a vertical mixing of buoyancy both inside the fjords and in the layered coastal water outside. If the coastal water is homogeneous, the intermediate layer is shallower. Baroclinic horizontal pressure gradients will support episodic water exchange between a stratified coastal ocean and fjords relatively frequent (Asplin et al., 1999).

Below sill-height, in the inner basins, one find the deep layer. This is the layer that is mostly affected by the dynamics caused by the presence of the sill. Sometimes there can be less replacement of water and therefore the state can be stagnant. The opposite state is called active state. This is when external currents are allowed to lift heavier seawater above sill level and into the basin, leading to renewal of the deep layer. However, if the fluctuations of external conditions are sufficiently strong, this inflow will be prevented, causing the deep water renewal to be intermittent (Gade and Edwards, 1980). At other conditions, the intrusion of seawater may be accelerated, leading to a maximum inflow. This is commonly known as overmixed conditions. Stigebrandt (1981) proposed this as a classification scheme for fjords. The fjords in this classifications tend to be characterized as two-layer systems, where the stratification is layered in two rather distinct levels. Normal fjords, or N-fjords, have constrictions that are deep relative to the upper layer thickness. When the

upper layer and lower layer approaches the same thickness, the result is maximum two-way transport, and the fjord is then a typical overmixed fjord, or O-fjord.

Between the fjord and the outer sea there are exchange processes, which are important because it determines how well ventilated the fjord is. If a fjord is poorly ventilated, they show a low dissolved oxygen concentration, which is bad for the ecosystem of the fjord. If enough dense water is lifted above sill level, the deep-water in the inner basins of the fjord can be renewed. Although, there can be substantial periods of time during each complete renewal of the deep water, ranging from the tidal cycle and up to several years. It has also been found that in general, fjords with deep sills more often are renewed in the winter, while shallower sills are renewed in the summer (Gade and Edwards, 1980).

Several mechanisms determine how water is exchanged between the fjord and the outer sea, where the most steady one is the effect of tides. They provide the system with energy, and this energy can under certain conditions be available for mixing. It can also create turbulence, which again can enhance the mixing processes. The sill is an example on a location where the tides can lose energy to other processes. Under the right conditions, the energy can be transferred into a hydraulic jump as it enters the inner basin. Under other conditions, a jet may arise on the lee side of the sill, which gives higher velocity and can create turbulence towards the fjord banks. As the tidal-driven flow crosses the sill, frictional effects must be taken into account, and internal waves may be created at sill-height. This can lead to a standing wave above the sill, but the waves may also propagate inward towards the head of the fjord, before either dissipating or being reflected when hitting the bottom or fjord walls further in. Such a process of a constant train of progressive internal waves created by the tide can lead to a slow but steady mixing of the fjord basin water, eventually making this water sufficiently light for a deep water renewal of denser water from outside (Stigebrandt and Aure, 1989).

When considering tides, it should also be mentioned that the available energy is larger during spring tides than during neap tides (Freeland and Farmer, 1980). This means that the effects of the tides are enhanced when at spring, compared to those at neap. There may also be noticeable differences in the effect depending on different properties during the tidal cycle. Hence, the general circulation is expected to vary within periods that coincides with the tidal cycle.

One of the main features when it comes to mixing in the brackish layer and accelerating or decelerating the transport in the upper water masses is the wind, acting mainly inwards or outwards of the fjord, depending on how broad the fjord is. The wind also have some periodical timeline, but not in the same dependable way as the tides. The wind can act strongly on the fjord at some times, and then

suddenly not be noticeable at all. In the summer, the wind is most often directed inwards because of the warm weather. There are also daily periods, with the sun warming the air above the water during the day, causing an inward breeze, and the cooling during the night leading to an outward wind. How strong the wind is can also be affected by how broad the fjord is, leading to an acceleration in wind speed in the narrower parts, and an deceleration where the fjord gets broader.

The stratification also plays an important role when it comes to the vertical mixing in the fjord. When water of lower density are lead down into denser water, vertical density gradients are put up according to the dynamic effects of the buoyancy frequency, also known as the Brunt-Väisälä frecuency.

Another mechanism for mixing, flow and upwelling in fjords is the effect of the Coriolis force. In narrow fjords, the effect might not be noticeable at all, while in larger and broader fjords one may expect to find evidence of its presence. To know how broad a fjord has to be to experience these effects, one may turn to the Rossby radius of the fjord. If the fjord's breadth is within the range of the Rossby radius, then Coriolis may play a role in the mechanics of the fjord. Because of the rotation, the fjord may have inflow on one side and outflow on the other. This can also lead to upwelling on one side and downwelling on the other, causing the layers to have a tilt across the width of the fjord.

Even though fjords can be better subjects to investigate than the open sea, it can be even better to scale problems and examine them in a laboratory. A particular case was done by Cuthbertson et al. (2017), when a tank experiment was done to see how flow behaves in a lock exchange experiment over a sill. In this thesis, the first goal is to see whether this experiment can be satisfactorily reproduced numerically, using a non-hydrostatic model. Then the knowledge of sill dynamics will be used to study how the flow behaves in the presence of the sill, and especially how it is affected by rotation and the choice of the Coriolis parameter.

2 The numerical model

2.1 Bergen Ocean Model

The Bergen Ocean Model (BOM) is a three-dimensional numerical ocean model solving the primitive hydrodynamical equations on a horizontal Arakawa C-grid and with terrain following sigma coordinates in the vertical (Berntsen, 2000). The prognostic variables of the BOM are three components of velocity, salinity, temperature, surface elevation and two variables representing turbulent length scale and turbulent kinetic energy. The BOM has an embedded turbulence closure submodel (Mellor and Yamada, 1982). The main equations solved by the BOM is described in section 2.1 below.

The BOM has been successfully used in fjords and coastal waters, both with and without the use of hydrostatic approach (Asplin et al., 1999; Berntsen, 2000; Avlesen and Berntsen, 2001; Berntsen et al., 2002; Keilegavlen and Berntsen, 2009).

Since this thesis will reproduce a laboratory tank experiment with limited spatial extensions, the non-hydrostatic version of BOM is used.

2.2 Basic Variables and Equations

The following equations are used to describe the variables as functions of the Cartesian coordinates. (Note that salinity and temperature are not prognostic variables in this model implementation.)

The continuity equation is

$$\nabla \cdot \vec{U} + \frac{\partial W}{\partial z} = 0, \tag{1}$$

with the vector $\vec{U} = (U, V)$, and W is the vertical velocity. ∇ is the operator $(\frac{\partial}{\partial x}, \frac{\partial}{\partial y})$.

The equation for conservation of mass is given by

$$\frac{\partial \rho}{\partial t} + \frac{\partial}{\partial x}(\rho U) + \frac{\partial}{\partial y}(\rho V) + \frac{\partial}{\partial z}(\rho W) = \frac{\partial}{\partial z}\left(K_H \frac{\partial \rho}{\partial z}\right) + F_\rho. \tag{2}$$

ρ is the density of the fluid, K_H is the vertical eddy diffusivity and F_ρ is the horizontal eddy diffusivity.

The momentum equations are given as

$$\frac{\partial U}{\partial t} + \vec{U} \cdot \nabla U + W\frac{\partial U}{\partial z} - fV = -\frac{1}{\rho_0}\frac{\partial P}{\partial x} + \frac{\partial}{\partial z}\left(K_M \frac{\partial U}{\partial z}\right) + F_x, \tag{3}$$

$$\frac{\partial V}{\partial t} + \vec{U} \cdot \nabla V + W\frac{\partial V}{\partial z} + fU = -\frac{1}{\rho_0}\frac{\partial P}{\partial y} + \frac{\partial}{\partial z}\left(K_M \frac{\partial V}{\partial z}\right) + F_y, \tag{4}$$

$$\frac{\partial W}{\partial t} + \vec{U} \cdot \nabla W + W\frac{\partial W}{\partial z} = -\frac{1}{\rho_0}\frac{\partial P}{\partial z} - \frac{g\rho}{\rho_0} + \frac{\partial}{\partial z}\left(K_M \frac{\partial W}{\partial z}\right) + F_z. \tag{5}$$

P is the pressure, K_M is the vertical viscosity, ρ_0 is a mean reference density. The friction force can be written componentwise as

$$F_x = \frac{\partial}{\partial x}\left(A_M \frac{\partial U}{\partial x}\right) + \frac{\partial}{\partial y}\left(A_M \frac{\partial U}{\partial y}\right), \tag{6}$$

$$F_y = \frac{\partial}{\partial x}\left(A_M \frac{\partial V}{\partial x}\right) + \frac{\partial}{\partial y}\left(A_M \frac{\partial V}{\partial y}\right), \tag{7}$$

$$F_z = \frac{\partial}{\partial x}\left(A_M \frac{\partial W}{\partial x}\right) + \frac{\partial}{\partial y}\left(A_M \frac{\partial W}{\partial y}\right), \tag{8}$$

$$F_\rho = \frac{\partial}{\partial x}\left(A_H \frac{\partial \rho}{\partial x}\right) + \frac{\partial}{\partial y}\left(A_H \frac{\partial \rho}{\partial y}\right). \tag{9}$$

The pressure at depth z is

$$P = g\rho_0\eta + g\int_z^0 \rho(z)dz + P_{NH}, \tag{10}$$

where P_{NH} is the non-hydrostatic pressure due to fluid motion. At each step, the P_{NH} is approximated by solving an elliptic equation, see Keilegavlen and Berntsen (2009).

An equation for η is found by integrating the continuity equation over depth,

$$\frac{\partial \eta}{\partial t} = -\left(\int_0^\eta \frac{\partial U}{\partial x}dz + \int_0^\eta \frac{\partial V}{\partial y}dz\right). \tag{11}$$

2.2.1 Boundary conditions

At the free surface, $z = \eta(x, y)$, we have

$$\rho_0 K_M(\frac{\partial U}{\partial z}, \frac{\partial V}{\partial z}) = (0, 0). \tag{12}$$

There are no volume fluxes through the side walls, and due to the staggered Arakawa C-grid, no conditions are used on the longitudinal flow. However, due to the short horizontal grid spacing, ideally a wall boundary layer should have been implemented (Pedlosky, 1982).

The vertical velocities at the free surface and the bottom are given below.

$$W_0 = U\frac{\partial \eta}{\partial x} + V\frac{\partial \eta}{\partial y} + \frac{\partial \eta}{\partial t}, \tag{13}$$

$$W_b = -U_b\frac{\partial H}{\partial x} - V_b\frac{\partial H}{\partial y}. \tag{14}$$

The effect of the bottom drag on horizontal velocities is given by

$$\rho_0 K_M \left(\frac{\partial U}{\partial z}, \frac{\partial V}{\partial z}\right) = (\tau_{bx}, \tau_{by}). \tag{15}$$

The bottom stress is given by

$$\vec{\tau_b} = \rho_0 C_D |\vec{U_b}| \vec{U_b}, \tag{16}$$

where the drag coefficient, C_D, is

$$C_D = max\left(0.0025, \frac{\kappa^2}{(ln(\frac{z_b}{z_0}))^2}\right), \tag{17}$$

and z_b is the distance of the nearest grid point to the bottom. The von Karman constant is $\kappa = 0.4$. The bottom roughness parameter is set to $z_0 = 0.01$ m. In the C-grid, the nearest point with information to the bottom is located half a grid length away. This drag coefficient is chosen to mimic the effect of the no-slip condition, while conserving the correct dynamics of the Ekman layer (Berntsen et al., 2016; Berntsen et. al, 2018).

3 The numerical experiments of the exchange flow

3.1 The laboratory set up

The experiments in Cuthbertson et al. (2017) were simulating a tank of length $x = 9.0$ m, width $y = 1.5$ m and depth $z = 1.2$ m. The sill has a trapezoidal shape, with the dimensions of length $l_s = 2.0$ m, the same width as the tank, $w_s = 1.5$ m, and height $h_s = 0.5$ m. The angle of the inclination of the sill is set at $\alpha_s = 26.57°$ (Figure 1).

The experiments were conducted in a large-scale facility at Laboratoire des Écoulements Géophysiques et Industriels (LEGI) in Grenoble. The tank was constructed within a circular basin, which itself is 13 m in diameter and 1.2 m deep. This allowed total water depths H of up to 1 m. This basin was filled with freshwater up to the given height H in each experiment, which varied between $0.85 - 1.0$ m. Then saline water was introduced at the lower 0.3 m of basin M, through a rectangular section occupying the whole width, by a gravity feed system. The freshwater was recirculated within the system by two centrifugal pumps. The ranges of saline and fresh water fluxes were $Q_2 = 2.64 - 6.94ls^{-1}$ and $Q_1 = 0 - 30ls^{-1}$, respectively.

3.2 The numerical set up

The numerical experiment is trying to replicate this set up, and the tank therefore has the same dimensions. There is a small difference, as the water outtake in the model is programmed in another manner. When doing the physical experiment, they had an bigger circular tank that surrounded the tank within the experiment such that the water could flow out from basin M and be recirculated into the tank again. Here some of the water will instead be taken out at the bottom of basin I, while some will be taken out at the top of basin M. However, the water that is taken out are not programmed to be recycled.

The grid resolution will be at 10 cm horizontally. The model applies mode-splitting. The three-dimensional time step is at 0.025 seconds, and there are 30 two-dimensional steps for each 3D step. The rotation parameter (Coriolis) f is adjusted so the Rossby number is unity meaning the advection terms and the rotational terms in the momentum balance have the same magnitude.

The number of grid cells are set at 93 in the horizontal X-direction, 17 in the horizontal Y-direction and 81 in the vertical.

At the bottom, the dynamic boundary condition requires a no-slip of the fluid. In BOM, the nearest measured velocity point is located half a grid length above the bottom. The no-slip condition cannot therefore be enforced directly, and must be

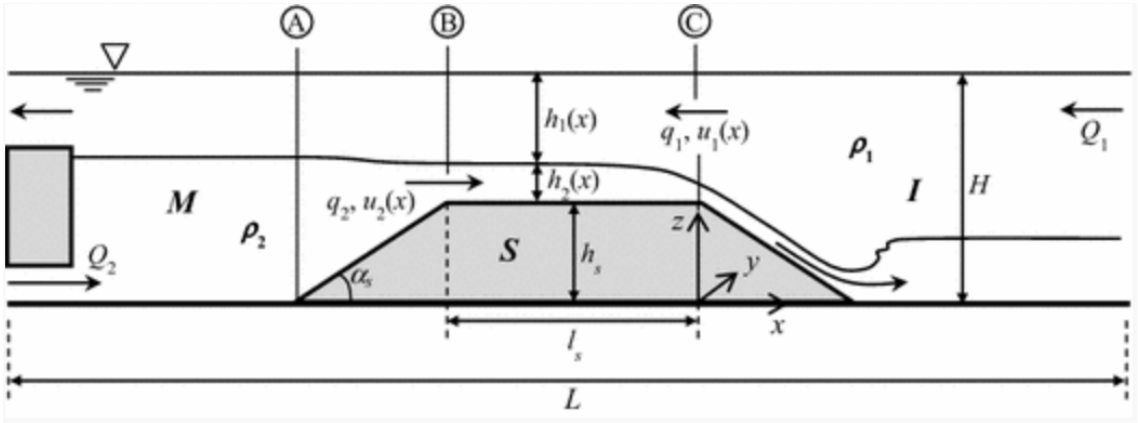

Figure 1: Courtesy of Alan Cuthbertson et al., "Blockage of saline intrusions in restricted, two-layer exchange flows across a submerged sill obstruction", (2017) (http://creativecommons.org/licenses/by/4.0/). M and I are the left and right basins, respectively. Q_2 and Q_1 are the saline and fresh water fluxes, respectively. L is the length of the channel and l_s is the length of the sill. The total water depth is H, while h_s is the sill height, h_1 is the depth of the upper layer and h_2 is the depth of the lower layer. α_s is the slope of the trapezoidal-shaped sill. ρ_1 and ρ_2 are the upper and lower layer densities, respectively, while q_1, u_1 and q_2, u_2 are the specific volume flux and the flow velocities.

implemented by the use of equation (16) in combination with equation (17), which mimics the effect of the condition. The flow can be described with a logarithmic function, which is the best approximation to how the flow behaves near the bottom (Berntsen et. al (2016)). Because of this, the denser water will be expected to form a plume, with a result that the denser water will be layered on top of the lower-density water at the head of the plume. This can lead to turbulence and mixing as the plume travels along the bottom.

3.2.1 FRS-zones - open boundary condition

To get satisfying results, it is necessary to apply relaxation to the ten outer grid cells on both sides of the tank. This is to assure that the flow is allowed be established as it enters the tank, which reduces the noise and turbulence made from the water entering. It also dampens the influence from the outtake, leading the water to flow out with a minimum of artificial numerical disturbances.

As an open boundary condition at the start and the end of the channel, the flow relaxation zone (FRS) is implemented. The FRS is, as mentioned, located at the ten outermost grid cells on each side of the channel, and the purpose is to have a smooth transition from the outer given solution to the internal values minimizing reflections and waves (Martinsen and Engedahl, 1987).

The equations are given by

$$U = (1 - \alpha)U + \alpha U_{relax}, \tag{18}$$

$$V = (1 - \alpha)V, \tag{19}$$

where

$$\alpha = \frac{\kappa \Delta t}{1 + \kappa \Delta t}. \tag{20}$$

U and V are the horizontal velocities in the x and y directions, respectively. The value U_{relax} is the velocity of the inflowing or outflowing water, while V is relaxed towards zero. The relaxation parameter, α, varies throughout the zone, with 0 at the start and 1 at the end.

In a corresponding way, the values of ρ are relaxed towards the density value of the inflowing or outflowing water masses in the FRS-zones.

3.2.2 Sub-grid scale closure

The horizontal 3D viscosity, A_M, and the 2D viscosity, A_{M2D}, were initially set to be

$$A_M = 2.0 \times 10^4,$$

and

$$A_{M2D} = 6.0 \times 10^{-1},$$

except for the areas near the inlet and outlet, where the horizontal 3D viscosity is increased to

$$A_M = 2.0 \times 10^{-2}.$$

These values were chosen to be large enough to minimize numerical noise, and small enough to allow the dynamics to be represented appropriately on the chosen grid. The vertical eddy viscosity and diffusivity are both set at constant values for each experiment, and the choice for these were made by doing numerical sensitivity studies, see chapter 4.1.

3.2.3 Control condition for transport capacity across a constriction

Stigebrandt (1981) showed that under steady conditions, there is an upper limit to the two-way transport capacity past a constriction. The control condition can be expressed as

$$\bar{F}_1^2 + \frac{\rho_1}{\rho_2}\bar{F}_2^2 = 1 \tag{21}$$

at the constriction, where $\bar{F}_1 = \bar{U}_1(g'h_1)^{-1/2}$ and $\bar{F}_2 = \bar{U}_2(g'h_2)^{-1/2}$ are similar to the densimetric Froude numbers for the two layers, $\bar{U}_1$ and $\bar{U}_2$ are the sectionally averaged flow speeds, and h_1 and h_2 are the upper and lower layer thicknesses, respectively. The reduced gravity is given by $g' = g\frac{\rho_2-\rho_1}{\rho_2}$, where ρ_1 and ρ_2 are the upper and lower layer densities.

3.3 The experiments

A total of 16 experiments were conducted with the purpose of reproducing the non-rotating results of Cuthbertson et al. (2017) and to include rotational terms to the same. The variables in the different experiments are listed in Table 1.

Experiments $1-4$ and $9-12$ will be referred to as the single-layered flow case, when the only water intake is the dense flow Q_2, and experiments $5-8$ and $13-16$ are the two-layered flow case, when a lighter water intake is included at the opposite end of the channel. The term $q^* = \frac{Q_1}{Q_2}$ is the fraction between the deep and dense inflow at the start of the channel and the lighter inflow at the end of the channel. The two cases will have values of $q^* = 0$ and $q^* = 4.32$ respectively.

The experiments are performed in a manner called lock exchange. The basic idea is that there is a gate in the middle of the channel dividing the basins. Upon removal, the setup of a semi-steady exchange of flow and counterflow between the

Experiment	Q_1 (ls^{-1})	Q_2 (ls^{-1})	f (s^{-1})	$\Delta\rho$ (kgm^{-3})	h_b (m)	K_M ($\mathrm{m}^2\mathrm{s}^{-1}$)	K_H ($\mathrm{m}^2\mathrm{s}^{-1}$)
1	0	6.94	-	5.1	0.43	3.0×10^{-5}	3.0×10^{-5}
2	0	6.94	0.0267	5.1	0.43	3.0×10^{-5}	3.0×10^{-5}
3	0	6.94	0.0534	5.1	0.43	3.0×10^{-5}	3.0×10^{-5}
4	0	6.94	0.01335	5.1	0.43	3.0×10^{-5}	3.0×10^{-5}
5	30	6.94	-	5.1	0.43	1.0×10^{-6}	1.0×10^{-6}
6	30	6.94	0.0267	5.1	0.43	1.0×10^{-6}	1.0×10^{-6}
7	30	6.94	0.0534	5.1	0.43	1.0×10^{-6}	1.0×10^{-6}
8	30	6.94	0.01335	5.1	0.43	1.0×10^{-6}	1.0×10^{-6}
9	0	6.94	-	4.7	0.349	3.0×10^{-5}	3.0×10^{-5}
10	0	6.94	0.0267	4.7	0.349	3.0×10^{-5}	3.0×10^{-5}
11	0	6.94	0.0534	4.7	0.349	3.0×10^{-5}	3.0×10^{-5}
12	0	6.94	0.01335	4.7	0.349	3.0×10^{-5}	3.0×10^{-5}
13	30	6.94	-	4.7	0.349	1.0×10^{-3}	1.0×10^{-6}
14	30	6.94	0.0267	4.7	0.349	1.0×10^{-3}	1.0×10^{-6}
15	30	6.94	0.0534	4.7	0.349	1.0×10^{-3}	1.0×10^{-6}
16	30	6.94	0.01335	4.7	0.349	1.0×10^{-3}	1.0×10^{-6}

Table 1: The experimental parameters.

basins is allowed. In this thesis, the flow or flows are in the same situation, except that the wall dividing the basins is replaced by inlets, which is closer to a natural scenario. More on the subject of lock exchange can be found in Whitehead (1998). The turbulence, mixing and mixing efficiency in exchange flow are closer described in Prastowo et al. (2008).

The water intake at the start of the channel has net volume flux $Q_2 = 6.94$ l s^{-1}. The intake is set to be in the lower 26 grid cells in basin M. This corresponds to approximately 0.3 m. On the opposite side, in basin I, there is an outgoing flow of the same net flux, occupying the same number of lower grid cells as in basin M. The tank is initially filled with freshwater up to 0.93 m. For the single-layered flow case, the vertical viscosity and the vertical diffusivity are both set to be constant 3.0×10^{-5} m^{2}s^{-1}. This is a result of initial experiments while varying these parameter values, and the chosen values give the most appropriate velocities.

For the two-layered flow case, Q_1 is gradually increased up to the point where $q^* = Q_1/Q_2 = 4.32$. When the flow Q_2 is about to enter the sill, Q_1 is released. This is done in the upper 36 cells of basin I. Simultaneously, an outtake of water in the upper 46 cells of basin M is initiated. This leads to a two-layered velocity system. In experiments $5-8$, the vertical viscosity and vertical diffusivity were both set to 1.0×10^{-6} m^{2}s^{-1} after initial trial experiments, which is lower than for the single-layered flow run, with $q^* = 0$. This demonstrates how sensitive the results were to these two mixing variables, which will be shown and discussed in section 4.1.

The density of the water taken in at Q_2 in experiments $1-8$ is $\rho_2 = 1005.1$ kg m^{-3}, making the density difference $\Delta\rho = 5.1$ kg m^{-3}.

The spatial dimensions of the channel will not be influenced by the Earth's rotation. However, in a fjord with a width exceeding a few kilometers, rotational effects can play a role, and this can be simulated by modifying the Coriolis parameter f. The Rossby number of the flow will be the fraction between the advective term and the rotation term in the momentum balance, and if the Rossby number is close to unity, rotation will be important for the flow. The Rossby number is given by the equation $Ro = \frac{U}{\Omega L}$, where U is the velocity scale, L is the length scale and Ω is the angular frequency rate. This is of the same order as the equation $Ro = \frac{U}{fL}$, where f is the Coriolis parameter. Assuming the Rossby number to be of order 1, the Coriolis parameter must have value $f = \frac{U}{L}$.

For the rotation to be equally important as the advection, the value of the Coriolis parameter should be $f = \frac{U}{L} = \frac{0.04}{1.5} = 0.0267$ s^{-1}. The velocity scale is chosen as the maximum mean velocity at the top of the sill, while the length scale is chosen as the width of the channel. Simulations are also done with $2 \times f = 0.0534$ s^{-1} and $\frac{f}{2} = 0.01335$ s^{-1} to test the sensitivity of f.

The difference between single-layered rotating systems, two-layered non-rotating systems and two-layered rotating systems is described in Pratt (2004).

Cuthberthsen et al. (2017) also did experiments where they made the flow across the sill more difficult (Ex7). To reproduce this with the numerical model, the maximum water depth is lowered to 0.849 m, and the sill depth is changed to 0.349 m. It is then less room above the sill for exchanging water, and the goal in this experiment is to see if the upper flow Q_1 can prevent the saline intrusion of climbing up above sill height. This phenomena is known as blocking. The density of the water at the intake Q_2 is now $\rho_2 = 1004.7$ kg m^{-3}, and the new density difference is then $\Delta\rho = 4.7$ kg m^{-3}. The water intake were done in the same way as in the first experiment, with the same number of cells per intake, same fluxes and the same gradually increased intake of Q_1. With this new geometry and water density difference, the eight first experiments were reproduced and listed as experiments $9 - 16$ in Table 1.

3.4 Sensitivity simulations

In order to test the sensitivity of the grid configuration and mixing parameter values, the basic experiments have been run a large number of times with different settings. The final set up used for the experiments in this thesis is a result of these sensitivity experiments.

4 The model results and discussion

4.1 Sensitivity studies

Note that the results from the sensitivity study are presented only for experiment 1 in Table 1.

The number of vertical grid cells and the mixing parameter values were important for the sensitivity of the results. Using 81 vertical grid nodes turned out to simulate the dynamics correctly. Using 21 cells gave numerical noise and did not solve the smaller dynamical features of the flow. The resolution was then increased to 41 grid cells, but this did not suffice either.

Taking a time average of the horizontal velocity U in each of the three cases approved the choice of vertical grid cells (Figure 2). When the number is at 21, the maximum velocity is below $U = 0.03$ ms^{-1}, and the plume has a thickness of about 0.1 m. This maximum is located at about $Z = 0.05$ m. Above $Z = 0.2$ m, there is a return flow reaching about $U = -0.005$ ms^{-1}.

The numerical results for when there were 41 vertical grid cells, shows a maximum velocity of beneath $U = 0.035$ ms^{-1}, just above a height of $Z = 0.05$ m. The plume then has a thickness approximately 0.1 m. Between $Z = 0.2$ m and the surface, there is a return flow where the velocity is at a little more than $U = -0.005$ ms^{-1}.

When adjusting the number of vertical grid cells to 81, the numerical results came out to be the most satisfying when comparing to the data from Cuthbertson et al. (2017). The maximum velocity is just above $U = 0.035$ ms^{-1}, located in the middle of $Z = 0.05$ m and $Z = 0.1$ m. The plume has a thickness of about 0.05 m. At a height of about $Z = 0.2$ m, the flow reaches zero velocity.

Throughout the experiments, the results were also shown to be quite sensitive to the values of the vertical eddy viscosity and the vertical eddy diffusivity, K_M and K_H respectively. By using the molecular values, K_M and K_H at 10^{-6} m^{2}s^{-1}, there is almost no mixing between the dense and lighter fluid masses. The pycnocline is very thin, the dense water flowing over the edge of the sill goes straight down and follows the bottom to the outtake without being mixed with the lighter water (Figure 3 (a)).

Increasing the values to 10^{-1} m^{2}s^{-1} creates so much vertical mixing that the whole water column gets the same density, decreasing inwards in the channel (Figure 3 (b)). The fluid also moves too slowly, so that after 750 seconds, the flow has yet to even reach the top of the sill.

After the same amount of time, the results with K_M and K_H at 3×10^{-5} m^{2}s^{-1}, shows a natural amount of mixing and movement in the channel, and these are therefore the values selected for the experiments 1 to 4 (Figure 3 (c)).

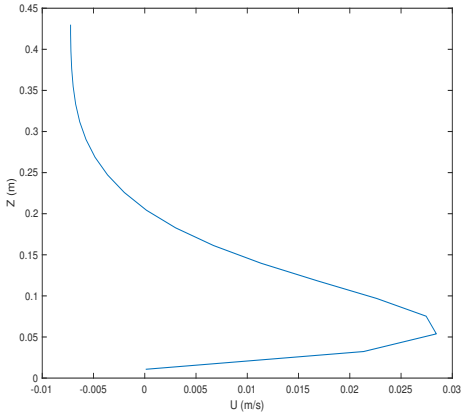

(a)

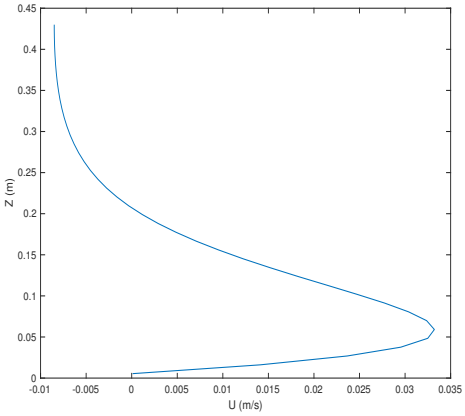

(b)

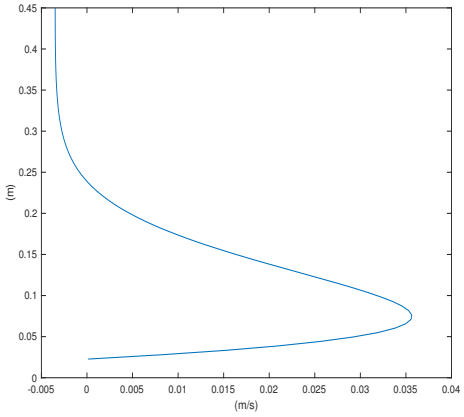

(c)

Figure 2: The plots show time averaged horizontal velocity when there are 21 vertical grid cells (a), 41 vertical grid cells (b), and 81 vertical grid cells (c).

Similar studies were done previous to all the experiments, and the selected values for K_M and K_H are listed in Table 1. The number of vertical grid cells were chosen to be 81 in all the experiments.

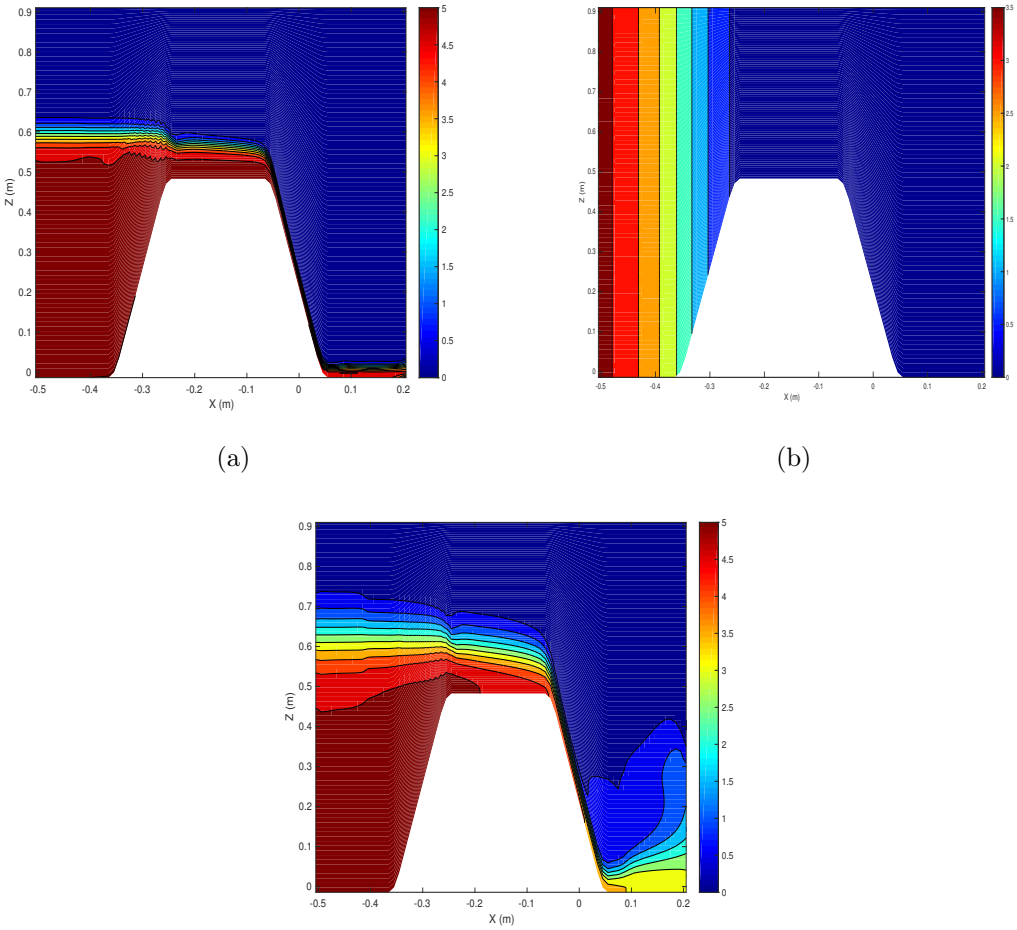

(a) (b)

(c)

Figure 3: Along-channel density-distribution after 750 seconds. (a) has $K_M = 10^{-6}$ and $K_H = 10^{-6}$, (b) has $K_M = 10^{-1}$ and $K_H = 10^{-1}$, and (c) has $K_M = 3 \times 10^{-5}$ and $K_H = 3 \times 10^{-5}$. The vertical axes show the depth Z in meters, while the horizontal axes show the length X in meters.

4.2 Experiments 1 to 8

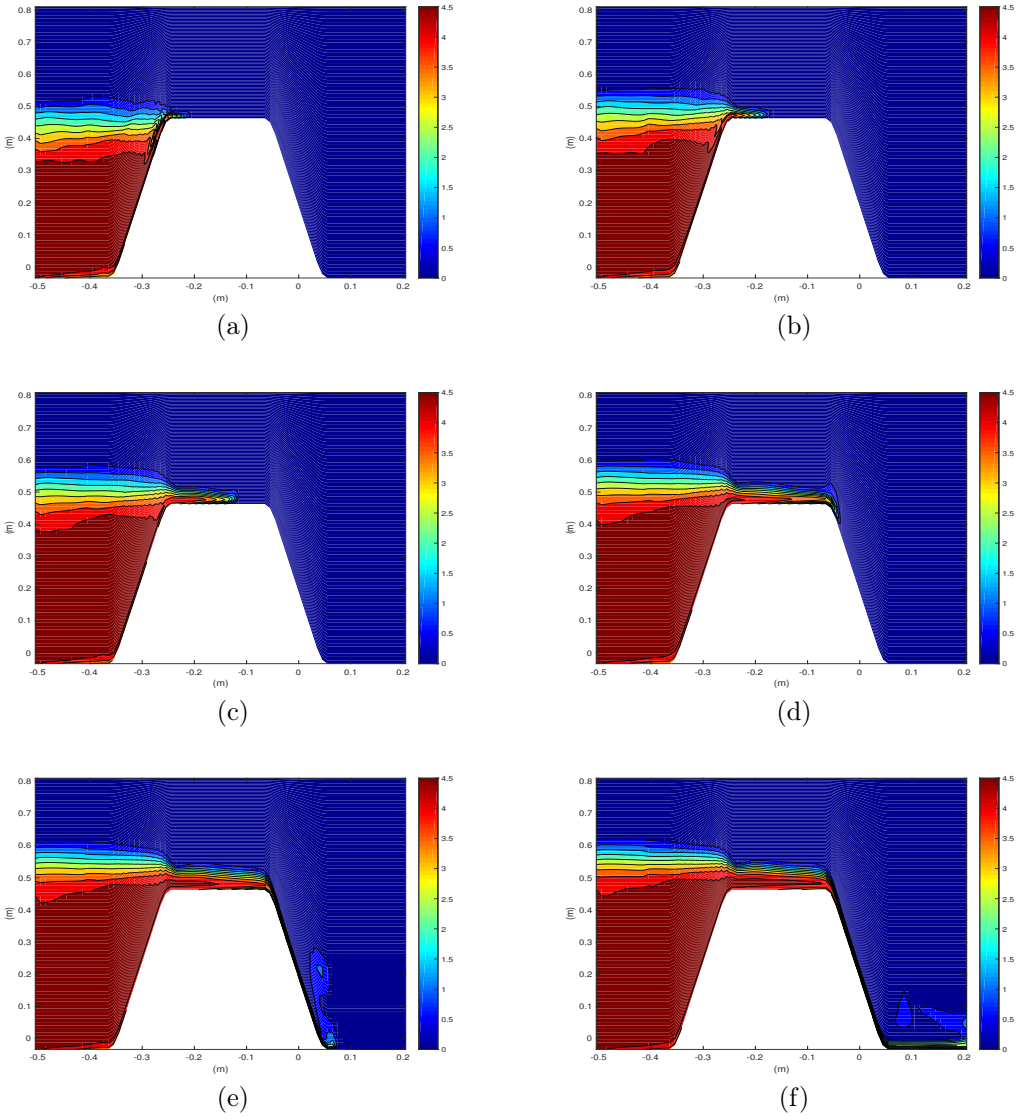

Figure 4: Along-channel density distribution from experiment 1 after 200 seconds (a), 225 seconds (b), 250 seconds (c), 275 seconds (d), 300 seconds (e), and 325 seconds (f). The horizontal axes show length X in meters, while the vertical axes show depth Z in meters.

When the dense water flow first enters the outer basin of the channel, some small oscillations occur. The interface between the dense and the lighter water masses has a height of between $0.15-0.20$ m while the first basin fills up. This indicates that there are some mixing between the two water masses. Upon approaching sill height, the dense water stabilizes, leading to smoother isopycnals. When the plume reaches the sill, the interface between the layers becomes sharper, indicating less mixing between the dense and light fluid. The plume is accelerated over the sill because of the depth difference (Figure 5). The plume has a distinct head, where the flow reaches a bit higher than in the body behind it, and with the previous mentioned denser water over lower-density water at the front. Due to buoyancy, this is an unstable situation, and mixing, entrainment and turbulence must be expected. While entering the inner basin I, the acceleration over the sill leads to a more mixed plume head, with less distinct density difference between the layers (Figure 4). During the descent into the inner basin, a tongue of denser water, with thickness of approximately 0.05 m, has risen about 0.20 m up in the inner basin. A hydraulic jump could have this effect on the flow. The flow should then jump up to a new height, and either stay at this height or have a gradually decrease. The condition for a hydraulic jump is that the flow is supercritical, that $Fr > 1$, before the jump, and then subcritical, $Fr < 1$, after. By taking the horizontal velocity U into account, the results show no sign of such a case (Figure 5). Turbulence and instabilities are more likely to be the case in this situation. At later times, this tongue has sunken down again, and is not visible in the data anymore, and the denser water is either mixed into the lighter water, or back into the flow along the bottom.

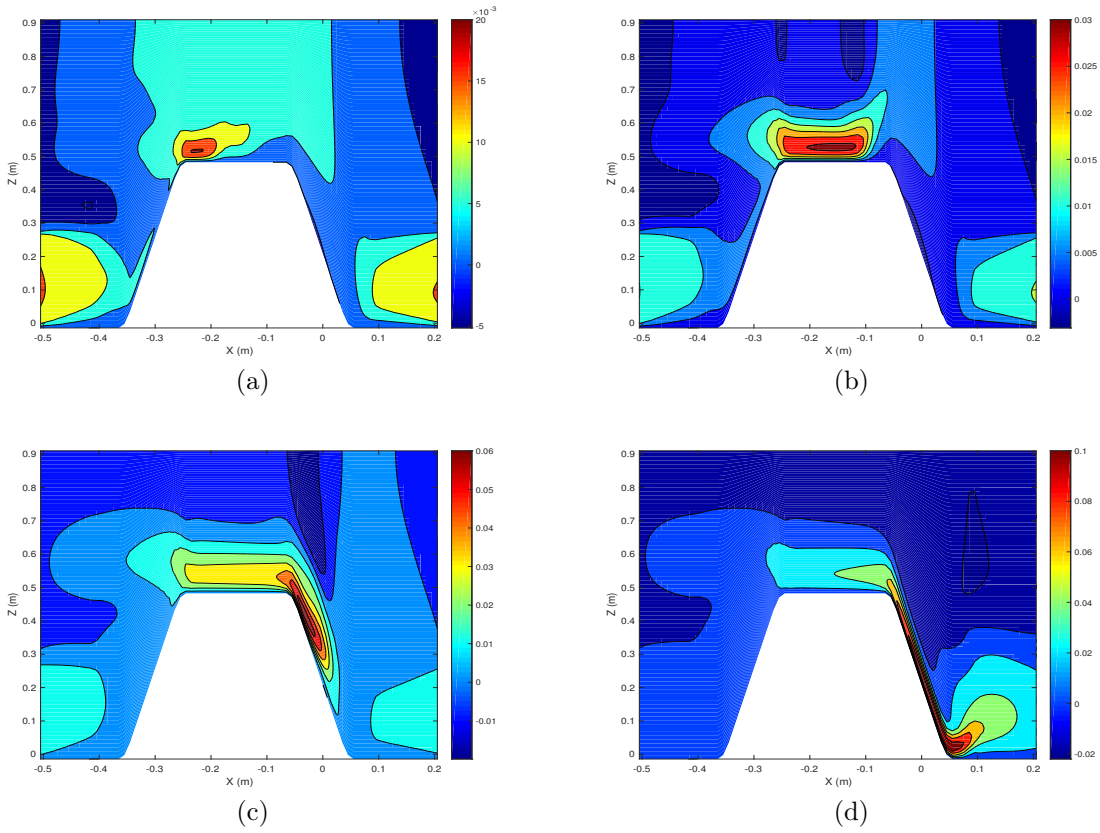

Figure 5: Along-channel velocity U in meter per second from experiment 1 after 200 seconds (a), 250 seconds (b), 300 seconds (c), and 350 seconds (d). The horizontal axes show length X in meters, and the vertical axes show depth Z also in meters.

A time series of the density-distribution at the top of the sill shows a smooth laminar plume (Figure 7). It is taken between 250 seconds, which is around the time frame for when the dense plume reaches the middle of the sill, up to nearly 650 seconds.

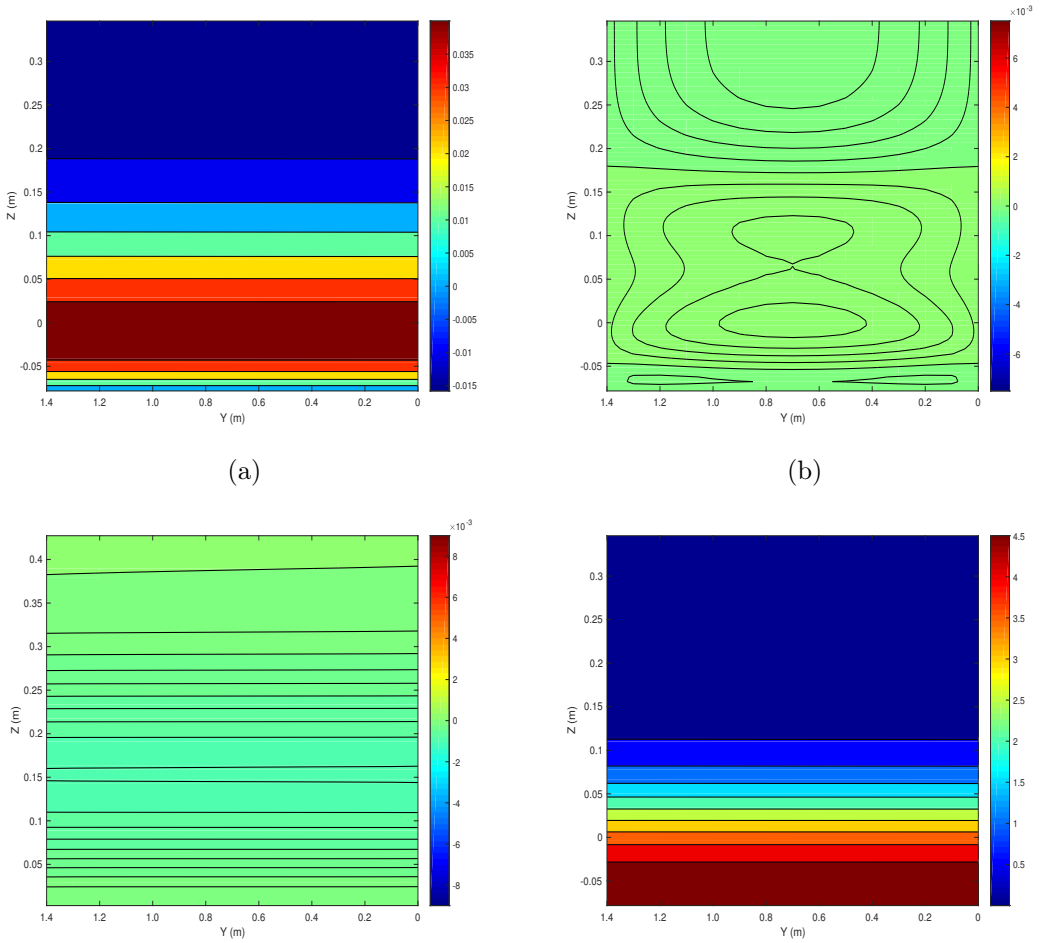

Figure 6: Across-channel results from the top of the sill after 500 seconds in the single-layered flow case without rotation (Experiment 1) of the horizontal velocity U (along-channel) in ms^{-1} (a), the horizontal velocity V (across-channel) in ms^{-1} (b), the vertical velocity W in ms^{-1} (c), and the density distribution (d). The horizontal axes show the length Y in meters (note the increasing values towards the left), while the vertical axes show the depth Z in meters.

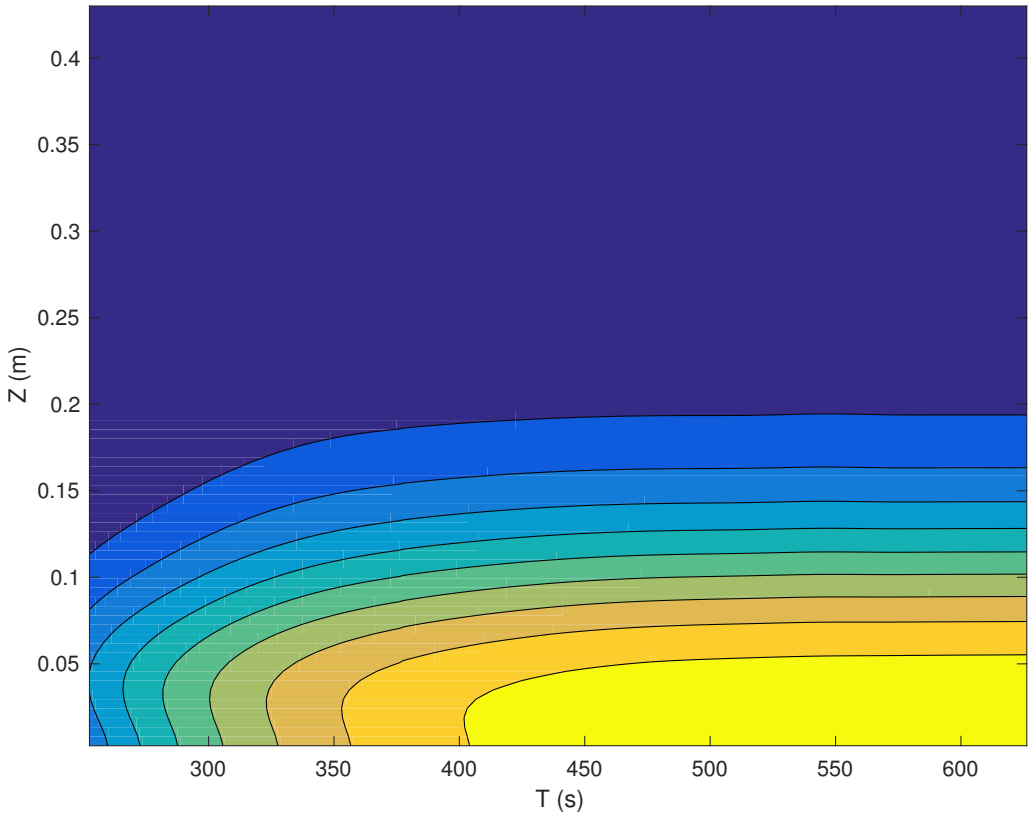

Figure 7: Time series of the density-distribution at the middle of the sill in the single-layered flow case without rotation (Experiment 1). The horizontal axis shows the time T in seconds, and the vertical axis shows the depth Z in meters.

For the purpose of comparison and for approving the hypothesis, the results of the velocities from Cuthbertson et al. (2017) has been included in this thesis.

The two experiments of Cuthbertson et al. (2017) that has been reproduced, are the two extremes. One with no inflow of fresh water (the single-layered flow case), and one with the most inflow of fresh water (the two-layered flow case). The numerical profiles (Figure 8) of the single-layered flow case and the two-layered flow case correspond to the black profile and the purple profile in the paper, respectively (Figure 9). The measurements in Cuthbertson et al. (2017) probably have some uncertainties due to the influence of the measurement devices, and the results from this thesis might also include some numerical errors. Taken this into account, the results from the numerical experiment and the physical experiment compares reasonably well.

The physical experiments show maximum velocities at the three locations along the sill of about $U = 0.038$ ms^{-1}, $U = 0.035$ ms^{-1} and $U = 0.038$ ms^{-1} for the single-layered flow case. The numerical experiments have results about $U = 0.035$ ms^{-1}, $U = 0.035$ ms^{-1} and $U = 0.045$ ms^{-1}, at the approximately same locations.

In the same way, the two-layered flow case for the physical experiment have results showing maximum velocities of about $U = -0.065$ ms^{-1}, $U = -0.06$ ms^{-1} and $U = -0.06$ ms^{-1}, at the beginning, middle and end of the sill, respectively. The numerical experiment show maximum velocities of about $U = -0.06$ ms^{-1}, $U = -0.06$ ms^{-1} and $U = -0.055$ ms^{-1} at the same locations. These are obviously from the flow Q_1. The maximum velocities of the lower plume from the flow Q_2 at the same locations in the physical experiments are $U = 0.038$ ms^{-1}, $U = 0.035$ ms^{-1} and $U = 0.05$ ms^{-1} respectively. The numerical experiments corresponding to these results show maximum velocities of $U = 0.03$ ms^{-1}, $U = 0.04$ ms^{-1} and $U = 0.045$ ms^{-1}.

In the numerical results, there are signs of a barotropic return flow above the plume in the case with no inflow of fresh water. It is most evident in the plot at the beginning of the sill, and almost not visible in the plot at the end of it. This is, however, not a trait of the physical results. Thus, it is probably a numerical error due to e.g. the boundary condition on the downstream side, where water exits the tank. The inflow may be stronger than the outflow, causing some of the water that enters the inner basin I to create a return flow in the upper part of the channel.

Altogether, the results from the physical and numerical experiments correspond relatively well, and we conclude that the numerical model implementation is sound. Further experiments in this thesis will then be assumed to be realistic and give reasonable outcomes.

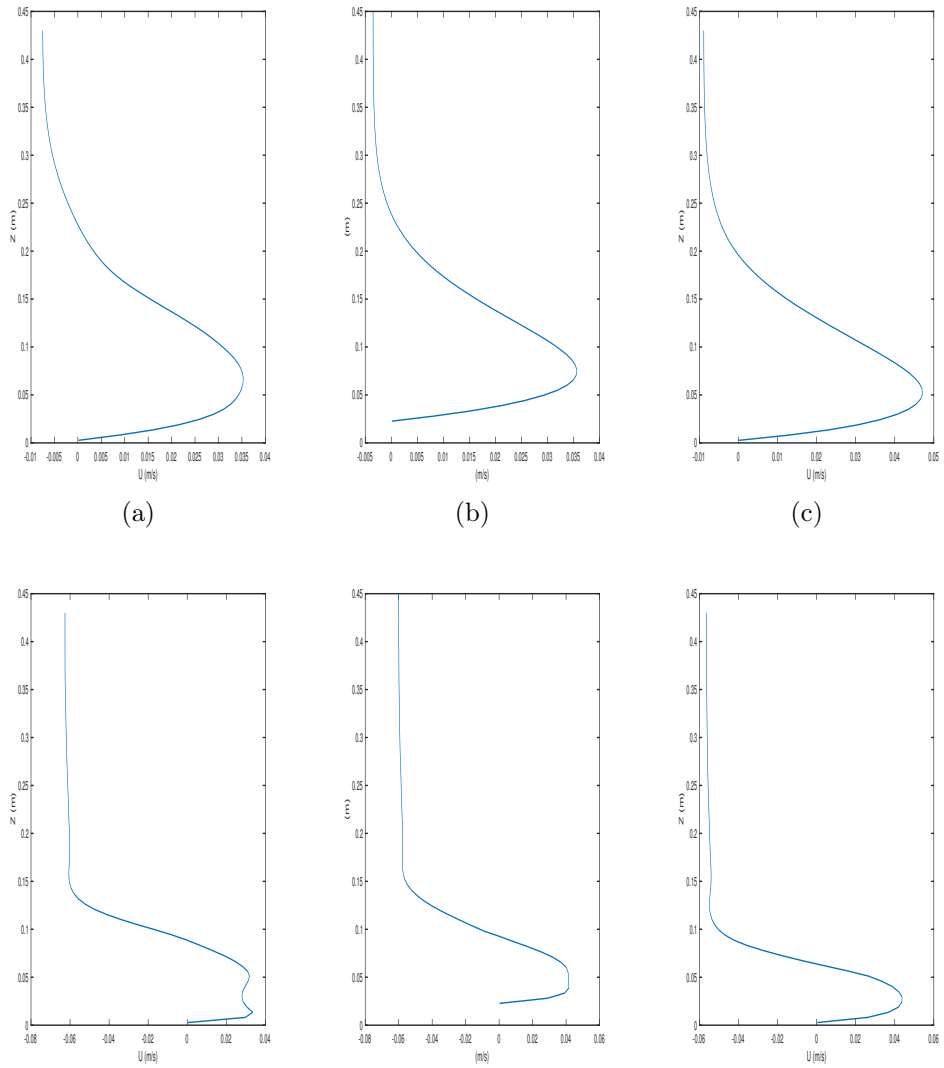

Figure 8: Time averages of the horizontal velocity taken at three locations at the top of the sill. The horizontal axes show the horizontal velocity U in meters per second, while the vertical axes show the depth Z in meters. They correspond to the two extremes from figure 7 (a) (i), (ii) and (iii) in Cuthbertson et al. (2017). The three upper plots, (a) - (c), are the single-layered flow case (Experiment 1), and the three lower plots, (d) - (f), are the two-layered flow case (Experiment 5). They show the velocity profiles at (a) and (d) the beginning of the sill, (b) and (e) the middle of the sill, and (c) and (f) the end of the sill.

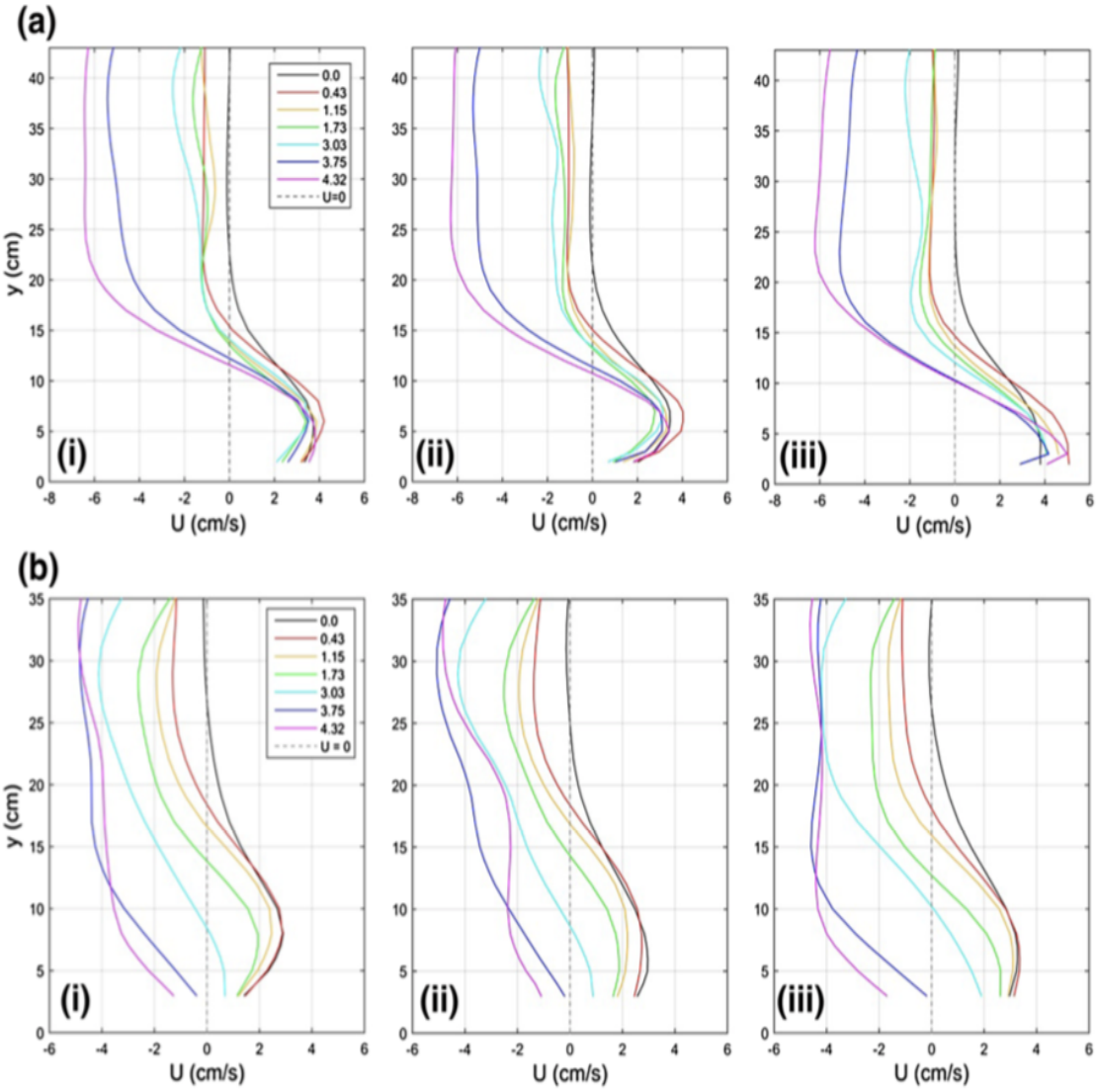

Figure 9: Figure 7 from Cuthbertson et al. (2017) Blockage of saline intrusions in restricted, two-layer exchange flows across a submerged sill obstruction. Horizontal velocity U in centimeter per second for (a) the single-layered flow case, and (b) the two-layered flow case with two incoming flows. Both (i) is taken at the beginning of the sill, the (ii) at the middle of the sill, and (iii) at the end of the sill. The horizontal axes show the horizontal velocity U in centimeters per second, and the vertical axes show the depth Z in centimeter.

4.2.1 Single-layered flow case

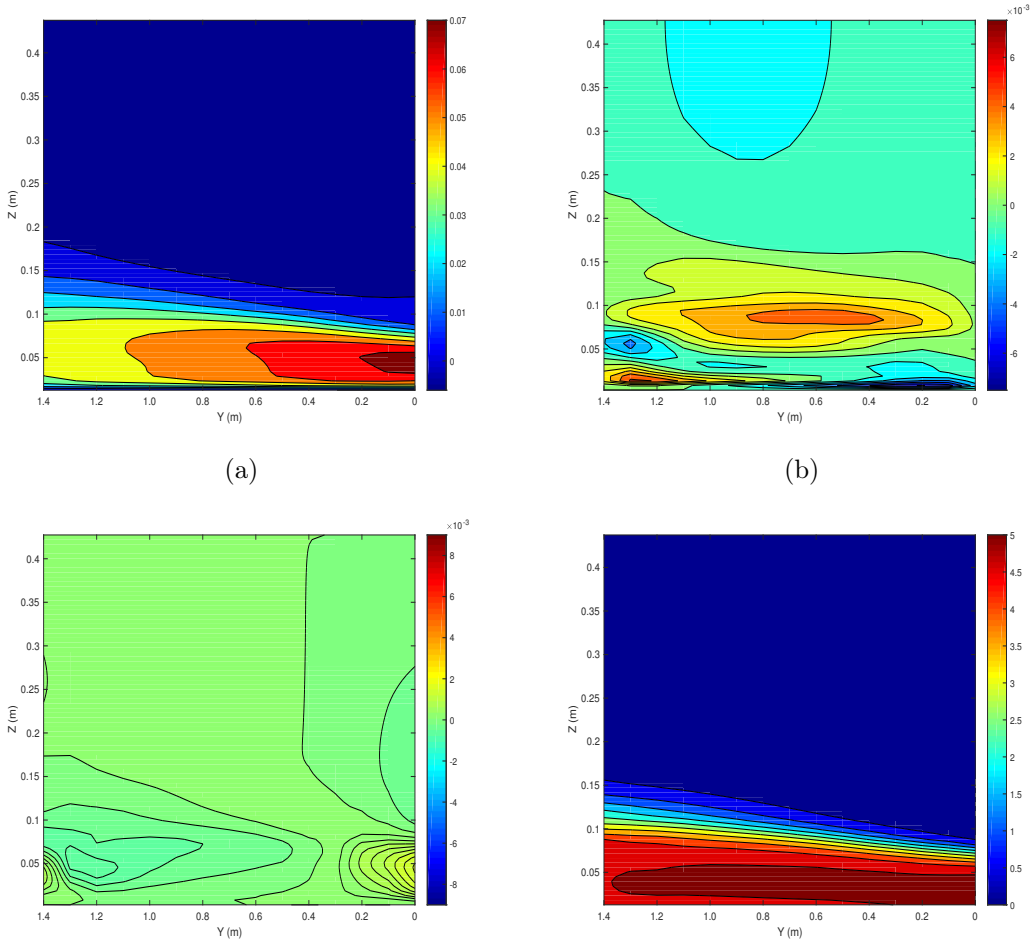

Figure 10: Across-channel results from the top of the sill after 500 seconds in the single-layered flow case with $f = 0.0267\ \mathrm{s}^{-1}$ (Experiment 2). (a) shows the horizontal velocity U in ms^{-1}, (b) shows the horizontal velocity V in ms^{-1}, (c) shows the vertical velocity W in ms^{-1}, and (d) shows the density-distribution. The horizontal axes show the width Y in meters, and the vertical axes show depth Z in meters.

The next step in this thesis is to investigate how the flow behaves when rotation is added. As described previously, the chosen value for the Coriolis parameter is

$f = 0.0267$ s^{-1}. The results show that rotation creates significant across-channel variations, in opposition to the case without rotation when these are non existent.

Results from the experiment without rotation, experiment 1, show that the flow does not vary across, and with no velocities in the Y-direction (Figure 6). With added rotation, there is a higher velocity in the along-channel X-direction on the right side compared to the left. The maximum velocity is $U = 0.07$ ms^{-1}. On the other side of the channel, the velocity is only at about $U = 0.04$ ms^{-1}. The rotation must then either accelerate the water on the right side of the channel, decelerate the water on the left side of the channel, or a combination of both. Similar results from when there are no rotation shows a maximum velocity of about $U = 0.035$ m/s, meaning the added rotation has the function of accelerating all the water across the width of the channel, with enhanced effect towards the right side.

The density distribution shows similar shape as the horizontal velocity U. Because of the accelerated velocity on the right side of the channel, the most dense water seems to be pulled towards the right side to replace some of the water that has moved away with the maximum velocity. Therefore, the most dense water is found along the bottom on the right side, and it is lifted slightly at $Y = 0.4$. Surrounding it is lighter water, which should lead to concerns regarding buoyancy forces. Another trait of the density distribution is that the denser water reaches higher on the left side, causing a slope downwards towards the right. This must also be an effect of the inflicted rotation, because of the balance between the Coriolis force and the pressure force. The circulation in the currents across the channel (Figure 10 (b)), show a positive net flow towards the left side in the dense layer, which could lead to the slope in the density-distribution. As should be expected, this slope can also be found in the horizontal velocity U, which confirms that the velocity follows the lifted dense water.

Adding rotation to the simulation introduces a transverse flow compared to the results without rotation. A second order clockwise circulation cell is established in the cross-channel plane. When the dense water is accelerated in the lower right corner, increased mixing takes place in the shear between the along-channel flow and the stagnant water above. This causes entrainment of lighter fluid into the dense current, which leads to a replenishment of the stagnant light fluid. This flow occurs as a rightward current in the upper 0.2 m of the channel, of maximum $V = -2 \times 10^{-3}$ ms^{-1}. The Coriolis force sets up a return flow towards the left side, with maximum velocity about $V = 4 \times 10^{-3}$ ms^{-1}, at a height of approximately $Z = 0.1$ m. The dynamics behind this transverse circulation cell does not seem to previously be described in the literature (B. Cushman-Roisin, pers. com.). The velocities across the channel are, however, relatively small compared to the along-channel flow, with a dividing factor of about 10^{-3}. Thus it is hard to explore, and this could be an

explanation of the lack of written descriptions. Similar results, but with flow in the Ekman layer and in the interface, and a return flow in the interior has been described previously, but only for the dense layer (Darelius, 2008; Davies et al., 2005; Umlauf and Arneborg, 2009; Umlauf et al., 2010).

Below this large circulation cell, there are some small areas of water with across-channel velocity. This is most likely small scale motion that is set up to fulfill the balance between the Coriolis force and the pressure force.

The effects of added rotation are even more evident when studying the time development of the dense plume at three long-sections across the width of the channel (Figure 11). Even though the velocity is greater on the right side of the channel, the slope in the boundary between the dense and fresh water masses causes the flow to reach the top of the sill earlier on the left side than on the right, and hence it also reaches the inner basin earlier. A possible explanation is that a geostrophic balance is struck between the pressure terms and the Coriolis terms, creating a tilt across the channel. This is causing the water on the left side of the channel to flow into the inner basin I before the water on the right side.

Numerical results seen from above the channel (Figure 12), show that after 300 seconds the along-channel velocity is at its maximum on the right side, which is also found in previous results. As should be expected, in the first part of the outer basin, there is a positive along-channel flow component. When reaching the start of the bottom of the sill, more of the movement is directed upwards, and the along-channel component then comes to a stop. At the top of the sill, U is accelerated because of the narrowing of the height of the channel, before it comes to a stop again when the water goes down into the inner basin. When reaching the bottom, the water continues along the channel towards the outlet (Figure 12 (a)).

The across-channel velocity shows that there is a current towards the left side on the sill (Figure 12 (b)). On both sides of the sill, the direction changes and there are two slightly stronger current towards the right side. This could also be an explanation on why there is a different displacement in time across the channel, and why there is a slope across the channel. Before reaching the sill, the along-channel velocity U is not yet accelerated, leaving the across-channel velocity V to be the strongest current. The water on the left side of the channel must therefore reach the sill, and hence the inner basin I, first.

In the outer basin M, there seems to be a clockwise rotation, and in the inner basin I there seems to be a counterclockwise rotation. This means that the geostrophic balance gives rise to two eddies, one cyclonic and one anticyclonic, respectively.

Table 2 shows some non-dimensional numbers for the single-layered flow case. ν is the kinematic eddy viscosity, f is the Coriolis parameter, L is the horizontal length

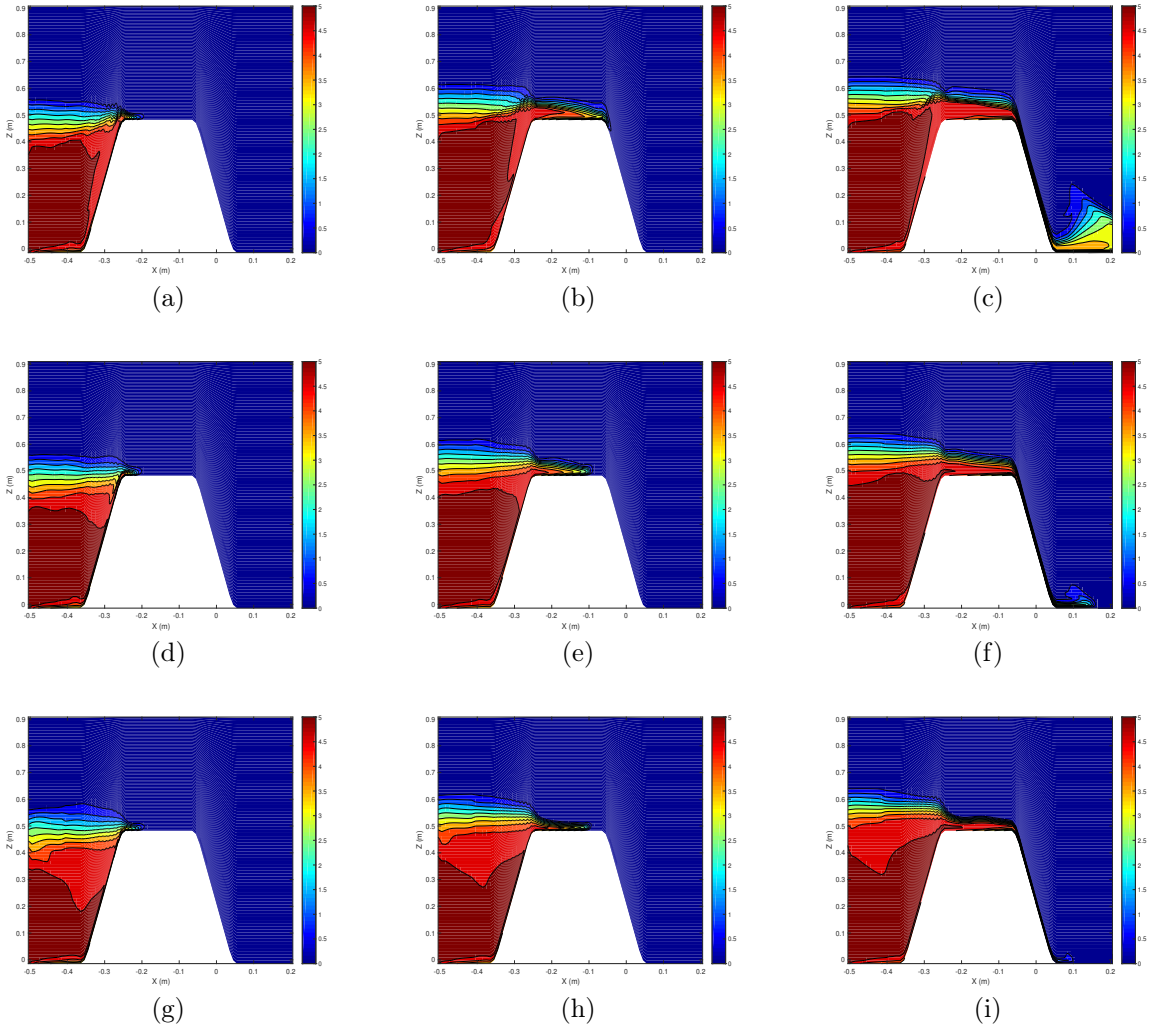

Figure 11: The density distribution in the single-layered flow case with $f = 0.0267$ s^{-1} after 200 seconds ((a), (d) and (g)), 250 seconds ((b), (e) and (h)) and 300 seconds ((c), (f) and (i)) (Experiment 2). The results are taken at three different locations across the channel: (a) - (c) is taken at the wall furthest from the viewing point, (d) - (f) from the middle of the channel, and (g) - (i) from the nearest wall. The horizontal axes show the length X in meters, while the vertical axes show the depth Z in meters.

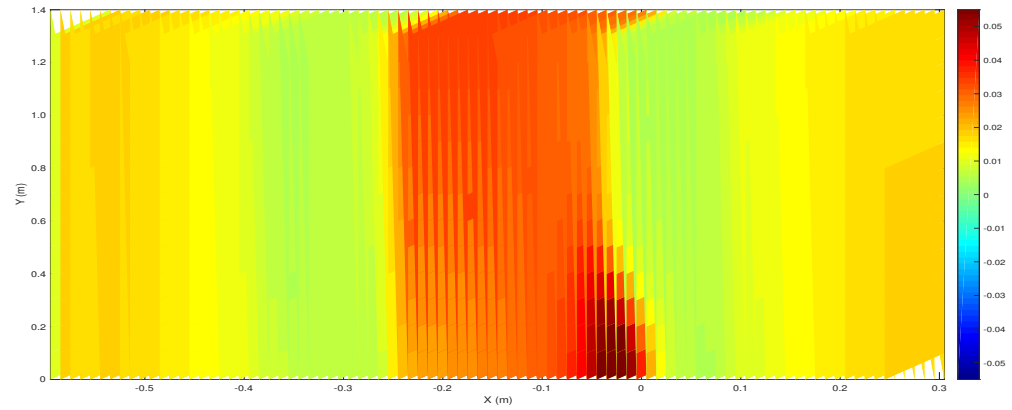

(a)

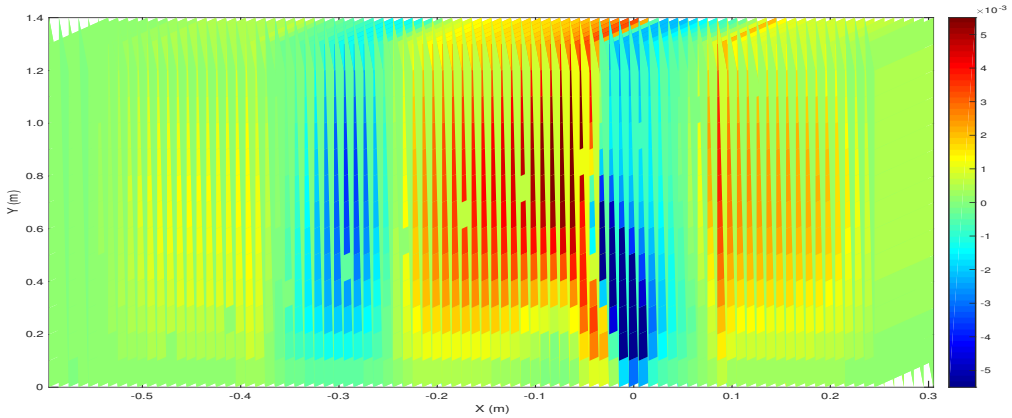

(b)

Figure 12: Horizontal velocity in the single-layered flow case after 300 seconds with $f = 0.0267$ s^{-1} (Experiment 2), along-channel U in ms^{-1} (a), and across-channel V in ms^{-1} (b). The horizontal axes show the length X in meters, and the vertical axes show the length Y in meters, meaning the figure are seen from above.

Ekman number	$Ek = \frac{\nu}{fL^2} = 5 \times 10^{-4}$
Rossby number	$Ro = \frac{U}{fL} = 1$
Temporal Rossby number	$Ro_T = \frac{1}{fT} = 0.08$
Reynolds number	$Re = \frac{UL}{\nu} = 2000$
Froude number	$Fr = \frac{U}{\sqrt{gH}} = 0.01$

Table 2: Non-dimensional parameters in the single-layered flow case (Experiment 2).

scale, U is the horizontal velocity scale, T is the timescale, H is the vertical length scale and g is the gravitational acceleration.

The Ekman number, which is the ratio of viscous forces to the Coriolis force, is small, but not as small as would be expected in an experiment of this scale. The number is between laboratory scale experiments (typical $Ek = 10^{-6}$) and geophysical flows (typical $Ek = 10^{-2}$) (Cushman-Roisin and Beckers, 2011), which should make the model useful for both purposes.

The turbulent length scales of the flow are related to the Reynolds number. This number implies the flow is at the border between laminar and transient flow, most likely towards the laminar side, as there is not much turbulence to be seen the channel.

The Froude number is relatively low, implying that the flow is subcritical. Slow and tranquil flow is a characteristic of this value.

4.2.2 Two-layered flow case

Similar tendencies as in the single-layered flow case can be seen in the results when the second flow is added.

The sloping in the results is still evident, but the presence of the upper stronger flow counteracts the height of the dense water plume across the whole width of the channel (Figure 13 (d)). The shear forces between the two flows going in opposite directions in the channel also effects the location of the maximum horizontal velocity U of the flow Q_2 in the tank, which is at about $U = 0.06$ ms^{-1} (Figure 13 (a)). While for the single-layered flow case the maximum U was located in the lower right corner, it is in the two-layered flow case displaced towards the left side of the tank,

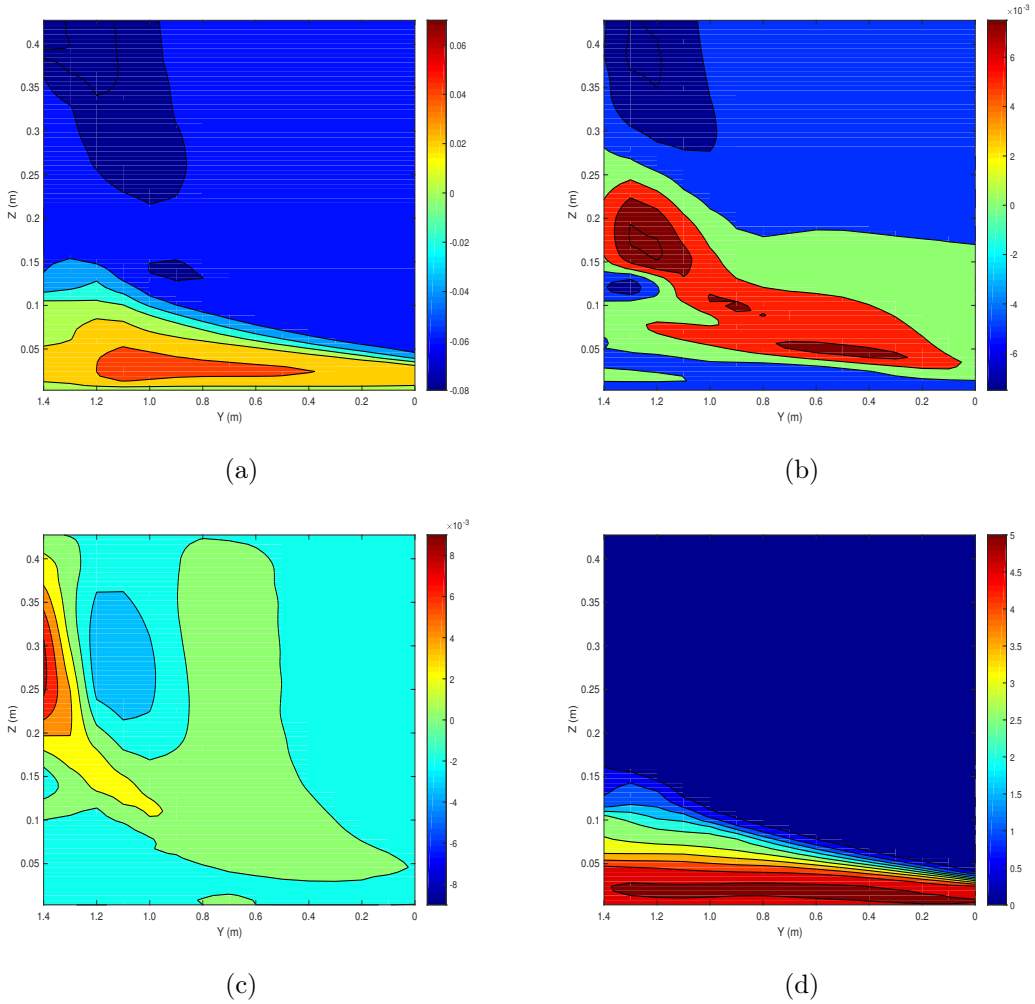

Figure 13: Across-channel results from the top of the sill after 500 seconds in the two-layered flow case with $f = 0.0267$ s^{-1} (Experiment 6). (a) shows the horizontal velocity U in ms^{-1}, (b) shows the horizontal velocity V in ms^{-1}, (c) shows the vertical velocity W in ms^{-1} and (d) shows the density-distribution. The horizontal axes show the width Y in meters and the vertical axes show the depth Z in meters.

between $Y = 0.4$ m and $Y = 1.2$ m. Other than that, the velocity of the flow Q_2 is relatively even in the horizontal, but follows the slope in the density-distribution. The relatively strong shear forces balances out the effect of the Coriolis force in the horizontal velocity U and, to a certain extent, also the density-distribution. There seems to be less mixing between the two flows of different density on the left side, because of a rather thick pycnocline.

The circulation cell in the horizontal velocity V, however, seems to be enhanced by the added flow Q_1, with velocities up to twice the values than in the single-layered flow case (Figure 13 (b)). The horizontal velocities are enhanced on the upper left side of the channel. The flow Q_1 has a maximum horizontal velocity U in the upper left corner of the channel, at about $U = -0.07$ ms^{-1}. Both the current towards the left and the current towards the right across the channel have maximums near the left side wall, at $V = 7 \times 10^{-3}$ ms^{-1} and $V = -7 \times 10^{-3}$ ms^{-1} respectively.

The vertical velocity is oriented upwards along the upper half of the left side wall, and downwards along the lower part. This could be the reason for the split in the leftwards velocity V, with a small area of rightwards velocity in between. The directions of the vertical velocity are results of the across-channel flow reaching the wall and being forced to divide into an upward current and a downward current (Figure 13 (c)).

4.2.3 Double value of the Coriolis parameter

For a better overview on how the choice of the Coriolis parameter influence the flow, the experiments were rerun with twice the original value. The new parameter is $f = 0.0534$ s^{-1}.

Across-channel results from the top of the sill are studied for comparison with the results from the simulation with the originally chosen Coriolis parameter. Like the previous results, these are also from 500 seconds into the numerical run.

As expected, the most prominent effect of doubling the value of the Coriolis parameter is that the rotational dynamics are enhanced. Considering the single-layered flow case first, it is noticeable that the fluid masses seems to be more mixed. The density-distribution shows lighter water than for the lower valued Coriolis parameter, with the densest water in the cross-sectional area at $\rho = 1004.5$ kgm^{-3}. The rotation also causes a slope in the denser water, but it is about twice the height than the previous results, hinting at the possibility that this sloping angle is proportional to the value of the Coriolis parameter. The thickness of the pycnocline shows variations in the mixing across the channel, with more mixed water on the left side than on the right. Higher mixing leads to a deepening in the most dense layer at the bottom, which is in the opposite direction than the sloping in the other layers. This is a reaction of the accelerated flow on the lower right side, pulling the most dense water along with it.

The horizontal velocity U follows the same distribution, with the maximum velocity in the lower right corner of the channel, which has a magnitude of about $U = 0.06$ ms^{-1}. This is close to the value in the results with the lower Coriolis parameter. A return flow can also be found in the upper part of the channel, with a maximum at the surface in the left corner, at about $U = -0.04$ ms^{-1}. The rotation could explain the leftward location, and the cause of the return flow could be the same as when describing the velocity profiles without rotation. That is, that the numerical boundary conditions are not sufficient when it comes to taking out the same amount of water as coming in at the inlet, such that some of the water creates a return flow when reaching the wall in the inner basin I.

The transverse circulation seems to occupy the whole depth of the cross-sectional area on top of the sill. Near the bottom, towards the right side of the channel, the water of positive velocity is located. The maximum positive velocity is at about $V = 0.01$ ms^{-1}. Surrounding this is a rather large area of zero velocity. At the surface, the water of negative horizontal velocity V is found, with a maximum at approximately $V = -0.02$ ms^{-1}. The surface current towards the right side of the channel is though twice as strong as the bottom current towards the left side. This could be the explanation on why there is a slope in the fields, where the water

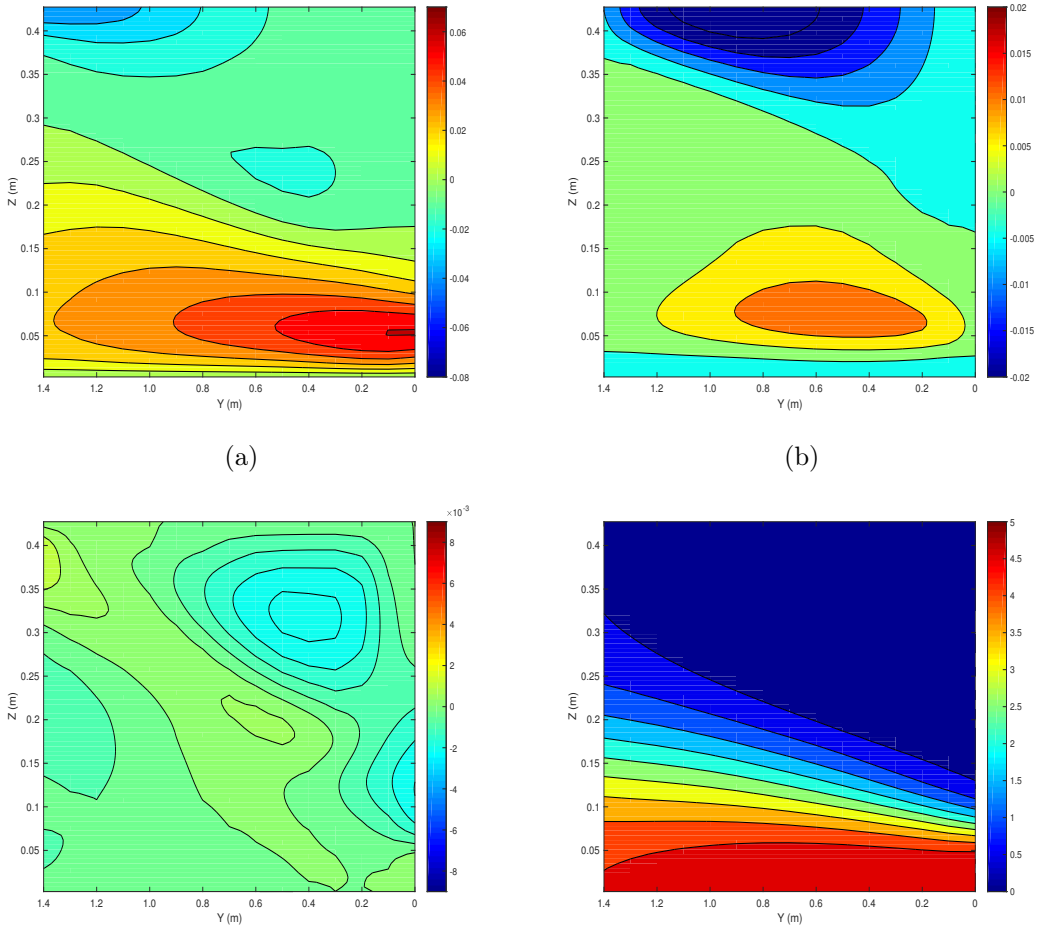

Figure 14: Across-channel results from the top of the sill after 500 seconds in the single-layered flow case with doubled Coriolis parameter, at $f = 0.0534$ s^{-1} (Experiment 3). (a) shows the horizontal velocity U in ms^{-1}, (b) shows the horizontal velocity V in ms^{-1}, (c) shows the vertical velocity W in ms^{-1}, and (d) shows the density-distribution. The horizontal axes show the width Y in meters, and the vertical axes show the depth Z in meters.

of rightwards velocity reaches down on the right side, and the zero velocity water reaches towards the surface on the left side. Another noticeable feature is that the currents are about ten times stronger than the ones with the lower Coriolis parameter, indicating that this is also an effect of the doubled rotation.

The results from double rotation in the two-layered flow case have the most prominent feature as an outcropping of the lighter water. The Coriolis force succeeds in pulling all the dense water towards the left of the channel. Stronger mixing occurs in the dense water masses, since there is only a thin layer of water of density $\rho = 1005.1$ kgm^{-3} found near the bottom. On the left side of the channel, the pycnocline is rather thick, while on the right side, there is a finer boundary between the dense and light water. This implies that there is more mixing and entrainment between the two flows towards the left side of the channel, but also vertical advection.

The horizontal velocity U towards the inner basin I, follows the outcropping seen in the results for the density-distribution, as would be expected. The maximum positive velocity is found towards the rightwards edge of the triangular shaped flow, and it is at approximately $U = 0.04$ ms^{-1}. The rest of the cross-sectional area of the channel has a current towards the outer basin M. The maximum velocity in this direction is located on the left side, from the upper left corner and reaching about 0.25 m downwards. It is at about $U = -0.08$ ms^{-1}, which is twice the strength of the current in the opposite direction. In this case, the velocities are the same as for $f = 0.0267$ s^{-1}, so the increased Coriolis parameter has though no impact on the strength of the along-channel flows.

The horizontal velocity V almost divides the channel in half between the upper left corner and the lower right corner, where all the water of leftwards velocity is located in the lower left part, and the water of rightwards velocity is found in the upper right part. They nearly create two separate triangles in the channel. The rotation is also here most likely the factor behind the incline of the positive velocity water on the left side, and the negative velocity water that almost reaches all the way down to the bottom on the right side. The maximums of the positive and negative velocities are found near the upper left corner, and they are at about $V = 0.02$ m/s and $V = -0.02$ ms^{-1}, respectively. The rotation is the reason behind the acceleration at the left side of the channel. The across-channel secondary circulation is in this case located towards the upper left corner of the channel.

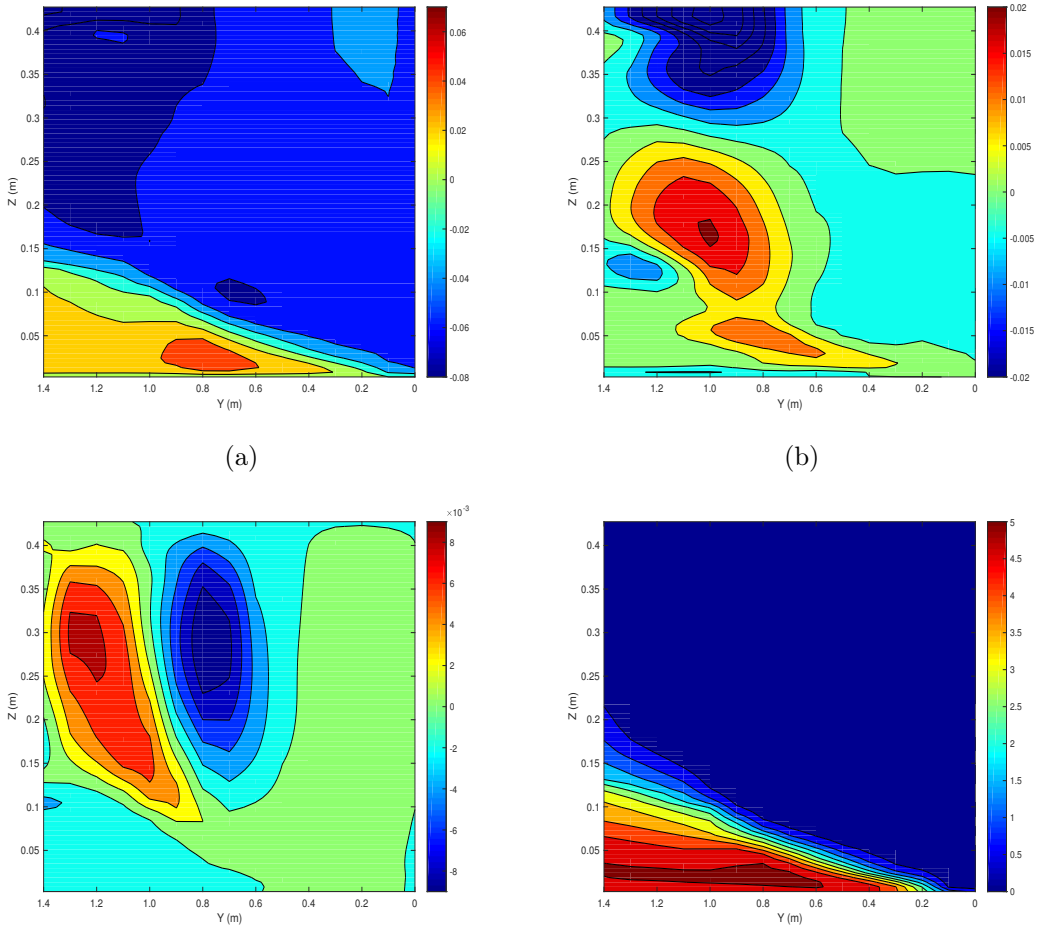

Figure 15: Across-channel results from the top of the sill after 500 seconds in the two-layered flow case with doubled Coriolis parameter, at $f = 0.0534$ s^{-1} (Experiment 7). (a) shows the horizontal velocity U in ms^{-1}, (b) shows the horizontal velocity V in ms^{-1}, (c) shows the vertical velocity W in ms^{-1}, and (d) shows the density-distribution. The horizontal axes show the width Y in meters, while the vertical axes show depth Z in meters.

4.2.4 Half the value of the Coriolis parameter

The rotational effects were also studied with the Coriolis parameter at half the chosen value, at $f = 0.01335$ s^{-1}. The results at a cross-sectional area at the top of the sill contradicts the previous assumed proportionality between the height of the slope and the Coriolis parameter. The angle of the slope is less than for $f = 0.0267$ s^{-1}, but the two water masses of different densities seems to be more mixed, such that the dense water reaches further up into the channel. A new theory could be a proportionality between the Coriolis parameter and the angle of the slope, but the differences in the three cases are quite small.

The slope in the density-distribution is very slug, and there is almost no variations in the mixing across the channel, as the pycnocline is of about the same thickness.

In the most dense water, at about $\rho = 1004.5$ kgm^{-3}, there is a slight downward slope at the left side wall, which is in the opposite direction than the rest of the water. The reason for this must be that the accelerated water on the right side of the channel is pulling on the most dense water.

The horizontal velocity U varies between $U = 0.04$ ms^{-1} and $U = -0.02$ ms^{-1}. The water of maximum negative velocity is located at the upper left corner, but water across the whole width of the cross-sectional area above $Z = 0.3$ m has negative velocity. This means that there is a return flow in the upper layer, intensified towards the upper left side because of the rotation. As in the other cases with a return flow, the reason behind is probably the boundary conditions that withdraws fluid. As expected, the positive velocity follows the slight sloping of the density-distribution, even the small slope in the opposite direction near the left side wall. The maximum velocity towards the inner basin, at $U = 0.04$ ms^{-1}, is located on the right side of the channel, right above $Z = 0.05$ m. As with the two other values of the Coriolis parameter, the current is accelerated on the right side of the channel, but only slightly, as expected for the low value of f. Otherwise, the rest of the current is not accelerated by this choice of the Coriolis parameter, indicating that a larger value is needed to accelerate the water across the whole width of the channel.

The results for the horizontal velocity V shows a rather weak transverse circulation cell, with a leftwards current in the lower part of the channel, and a rightwards current in the upper part. The maximum rightwards current in the upper part, at about $V = -4 \times 10^{-3}$ ms^{-1}, is located at the surface near the middle of the channel, but slightly towards the left. The maximum leftwards current, at about $V = 3 \times 10^{-3}$ ms^{-1}, is also located in the middle of the channel, but slightly towards the right. The water mass of positive horizontal velocity V is slightly shaped like the figure eight, more prominent on the left side. This could be a result of vertical velocities when the current reaches the left side wall, forcing it to split such that some of it continues

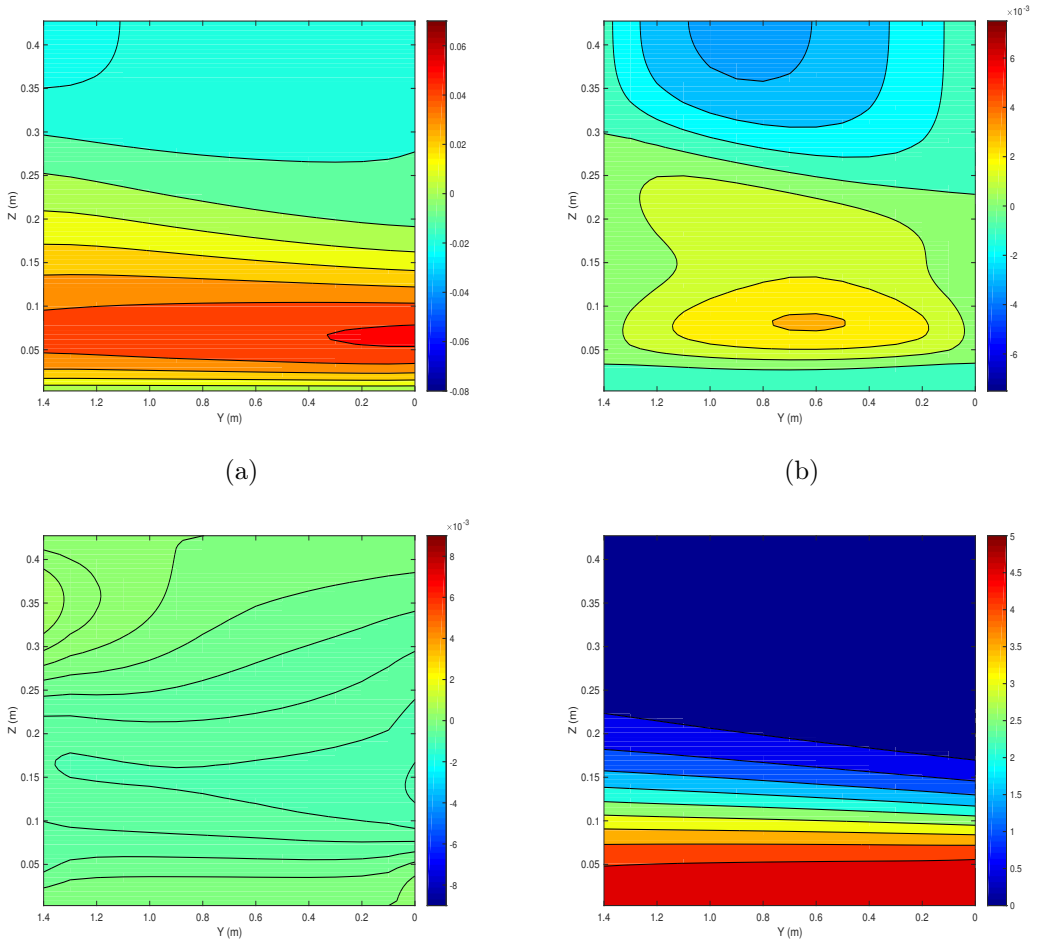

Figure 16: Across-channel results from the top of the sill after 500 seconds in the single-layered flow case with halved Coriolis parameter, at $f = 0.01335$ s^{-1} (Experiment 4). (a) shows the horizontal velocity U in ms^{-1}, (b) shows velocity V in ms^{-1}, (c) shows the vertical velocity W in ms^{-1}, and (d) shows the density-distribution. The horizontal axes show the width Y in meters, while the vertical axes show the depth Z in meters.

down and some continues up, and by that supplying the rightwards current above. The limit between the two currents has a slope, laying about 0.05 m above the tilted pycnocline in the density-distribution. The rotation must be the reason behind this shear in velocity.

Adding the second flow, Q_1, gives a quite different outcome. Almost no sloping is visible in the density-distribution, except for in the water that is just denser than the fresh water, where a tilt in the fluid can be noticed. The most dense water, at about $\rho = 1005$ kgm^{-3}, seems to be pulled towards the right side of the channel, being lifted away from the bottom and about 0.1 m from the left side wall. The layer is also thicker on the right side, probably increased by the dense water coming from the left side of the channel. The thickness of the pycnocline indicates that there are more mixing on the left side of the channel than on the right, as it is thicker on the left side.

The sloping in the horizontal velocity U follows that of the density-distribution. The maximum velocity towards the inner basin I, at about $U = 0.04$ ms^{-1}, is located next to the left side wall, below $Z = 0.05$ m. This is the opposite effect than for the single-layered flow case. The thicknesses of the layers of velocity are larger on the left side than on the right, backing up the theory of more mixing on the left side of the channel. The maximum velocity towards the outer basin M, at about $U = -0.07$ ms^{-1}, is located in the upper left corner, reaching all the way down to $Z = 0.15$ m along the left side wall, and with a thickness of about 0.4 m. The pull towards the left side must be an effect of the rotation in the channel.

The horizontal velocity V shows the same transverse circulation cell as seen in the other experiments. The upper half of the channel has rightwards velocity, with a maximum of about $V = -4 \times 10^{-3}$ ms^{-1} located at the surface in the middle of the channel, however slightly towards the left side. Beneath this is a layer of leftwards velocity, with a maximum of about $V = 6 \times 10^{-3}$ ms^{-1} located beneath $Z = 0.1$ m in the middle of the channel. In the middle of this layer of positive horizontal velocity V, there is a small area of relatively high negative velocity right by the left side wall, at about $V = -5 \times 10^{-3}$ ms^{-1}. The reason behind this must lay in the balance between the Coriolis force and the pressure force in the momentum equation.

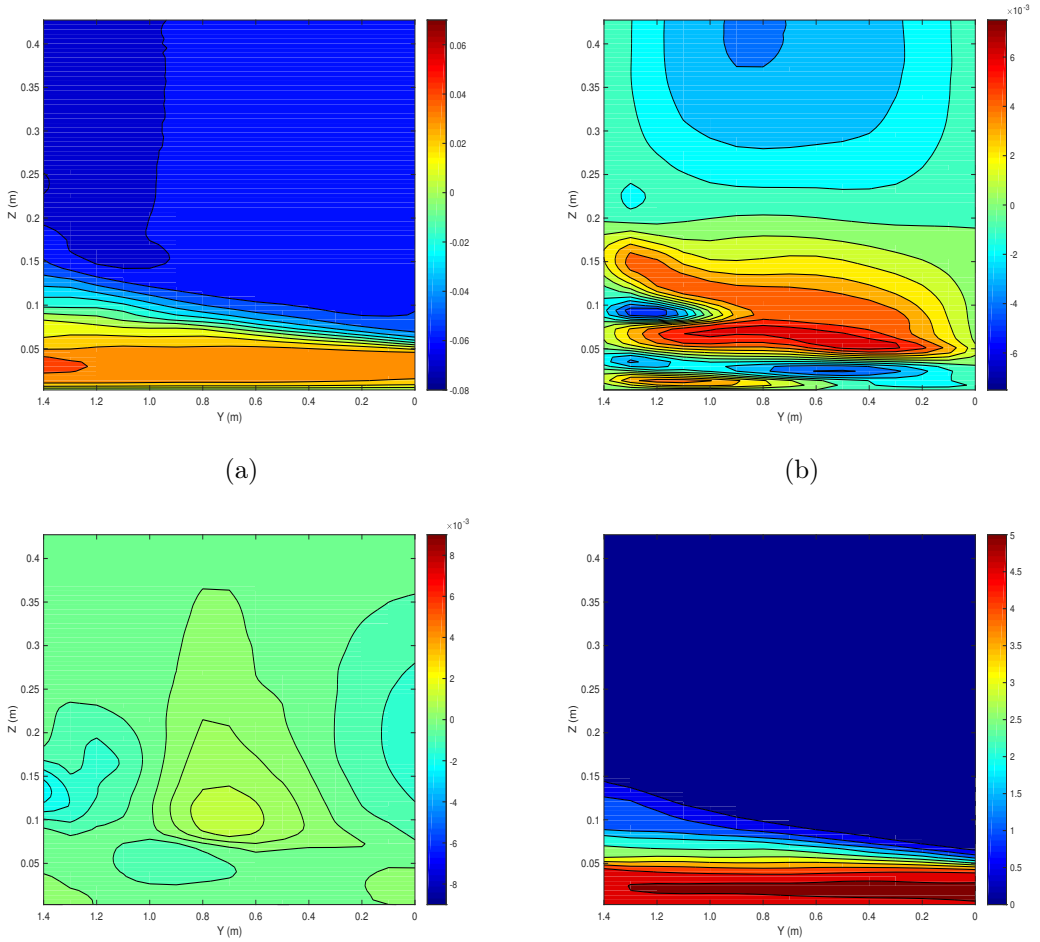

Figure 17: Across-channel results from the top of the sill after 500 seconds in the two-layered flow case with halved Coriolis parameter, at $f = 0.01335$ s^{-1} (Experiment 8). (a) shows the horizontal velocity U in ms^{-1}, (b) shows the horizontal velocity V in ms^{-1}, (c) shows the vertical velocity W in ms^{-1}, and (d) shows the density-distribution. The horizontal axes show the width Y in meters, and the vertical axes show the depth Z in meters.

4.3 Experiments 9 to 16

Now simulations of flow in a channel with shallower sill and less density difference between the water masses are performed, corresponding to Ex7 in Cuthbertson et al. (2017). With this configuration, blocking of the saline intruding flow occurred.

In the single-layered flow case, the velocity profiles do not show much difference between the experiments 1 and 9. The velocity varies between $U = 0.03$ ms^{-1} at the beginning of the sill, to $U = 0.04$ ms^{-1} at the end of the sill. These values are also in the same range as the profiles from Cuthbertson et al. (2017) (Figure 9 (b) (i) - (iii)). As in experiment 1, the numerical results show a small return flow in the upper part of the channel. This could be an effect of numerical error due to the boundary condition. The inflow may have higher velocity than the water at the outtake, causing the current to pile up water which in turn create a return flow in the channel when reaching the wall in the inner basin I.

The most significant difference between the two experiments occurred in the two-layered flow case. The lowered water height gave too little space above the sill for the flow Q_2 to climb over sill height, which is occupied by the stronger flow Q_1. In the results from the middle of the sill, this appears as velocity only in the negative X-direction. This phenomena is known as blocking of the saline intrusion.

Because of the inflicted zero-velocity at the bottom due to the imitation of the no-slip condition, the numerical results show an exponential curve in the velocity U, which is greatest at the surface. The smoothness of the curve indicates that in this choice of parameters, some small-scale dynamics are perhaps not modeled properly, at least in comparison with the results from Cuthbertson et al. (2017). However, these variations in the smoothness of the curve are so small that they could also be results of measurement errors in the physical experiments. The most important factor is, however, the ranges of the velocities, which indicates that, overall, the dynamics are correct.

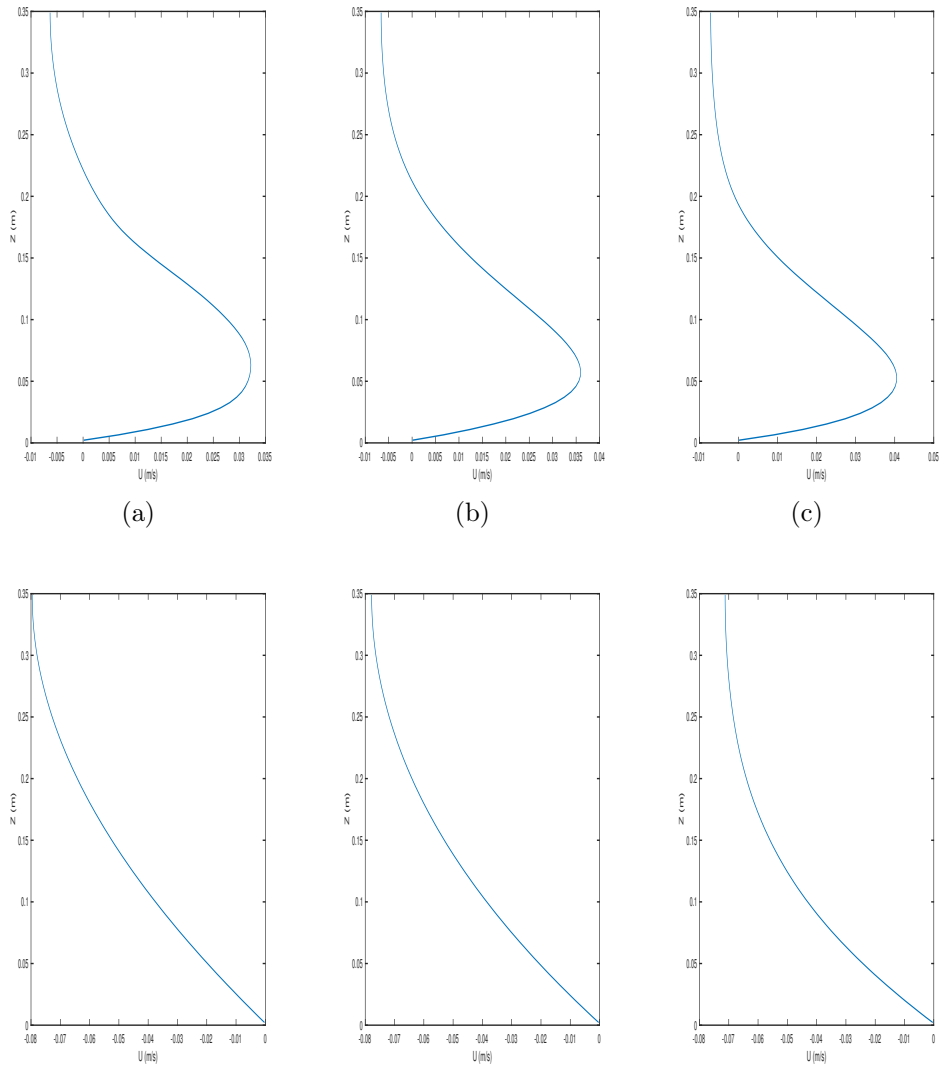

Figure 18: Time averages of the horizontal velocity taken at three locations at the top of the sill. The horizontal axes show the horizontal velocity U in meters per second, while the vertical axes show the depth Z in meters. They correspond to the two extremes from figure 7 (b) (i), (ii) and (iii) in Cuthbertson et al. (2017). The three upper plots, (a) - (c), are the single-layered flow case (Experiment 9), and the three lower plots, (d) - (f), are the two-layered flow case (Experiment 13). They show the velocity profiles at (a) and (d) the beginning of the sill, (b) and (e) the middle of the sill, and (c) and (f) the end of the sill.

4.3.1 Single-layered flow case

Rotational effects on the flow are also of interest in the single-layered flow case with the new bottom matrix and density difference. As for the first experiment, runs were done with $f = 0.0267$ s^{-1}, $f = 0.0534$ s^{-1} and $f = 0.01335$ s^{-1}.

Results from an cross-sectional area of the channel at the middle of the sill show more mixing with $f = 0.0267$ s^{-1} than in the corresponding experiment 2. The most dense water, at about $\rho = 1004.5$ kgm^{-3}, seems to be pulled towards the lower right corner, where the horizontal velocity U is the highest (Figure 19 (d)). The high velocity leads dense water along the channel, and the dense water reaching towards the right corner is probably to compensate for this. As in the first experiments, there is a slope in the layers of dense water, and these are thicker on the left side than on the right, which means that the vertical mixing is higher on the left side. This is causing the distinct slope in the density-distribution, and could also be a factor to why there is more dense water on the right side than on the left.

In the results of the horizontal velocity U, a return flow can be found in the upper left corner of the cross-sectional area (Figure 19 (a)). It has a maximum at about $U = -0.04$ ms^{-1}. The maximum positive velocity is located on the right side of the channel, at about $U = 0.04$ ms^{-1}. The rotation causes this accelerated flow at the right side.

A transverse circulation cell can also be found in the results for the horizontal velocity V in this case (Figure 19 (b)). The limit between the two layers have a slope, which is consistent with the sloping in the density-distribution. In the lower part of the channel, the positive leftward flow is located, with a maximum of about $V = 6 \times 10^{-3}$ ms^{-1}. The maximum is in the middle of the lower part of the channel, slightly towards the right side. On the left side of the area of water of positive velocity, there is a figure eight shaped curve, which can be explained by the upwards and downwards velocities near the left side wall (Figure 19 (c)). The upper negative flow towards the right side has a maximum velocity at about $V = -7 \times 10^{-3}$ ms^{-1}, located at the surface in a area much larger than the maximum positive velocity. It is in the middle of the channel, slightly towards the left side. These offsets from the middle seems to be an effect of the slope between the two layers, which in turn is created by the rotation. Both the positive and negative velocities are higher than in experiment 2, which is at $V = 4 \times 10^{-3}$ ms^{-1} and $V = -4 \times 10^{-3}$ ms^{-1}, respectively. The smaller passage between the surface and the sill must create an acceleration in the transverse velocity, or it enhances the effect of the rotation.

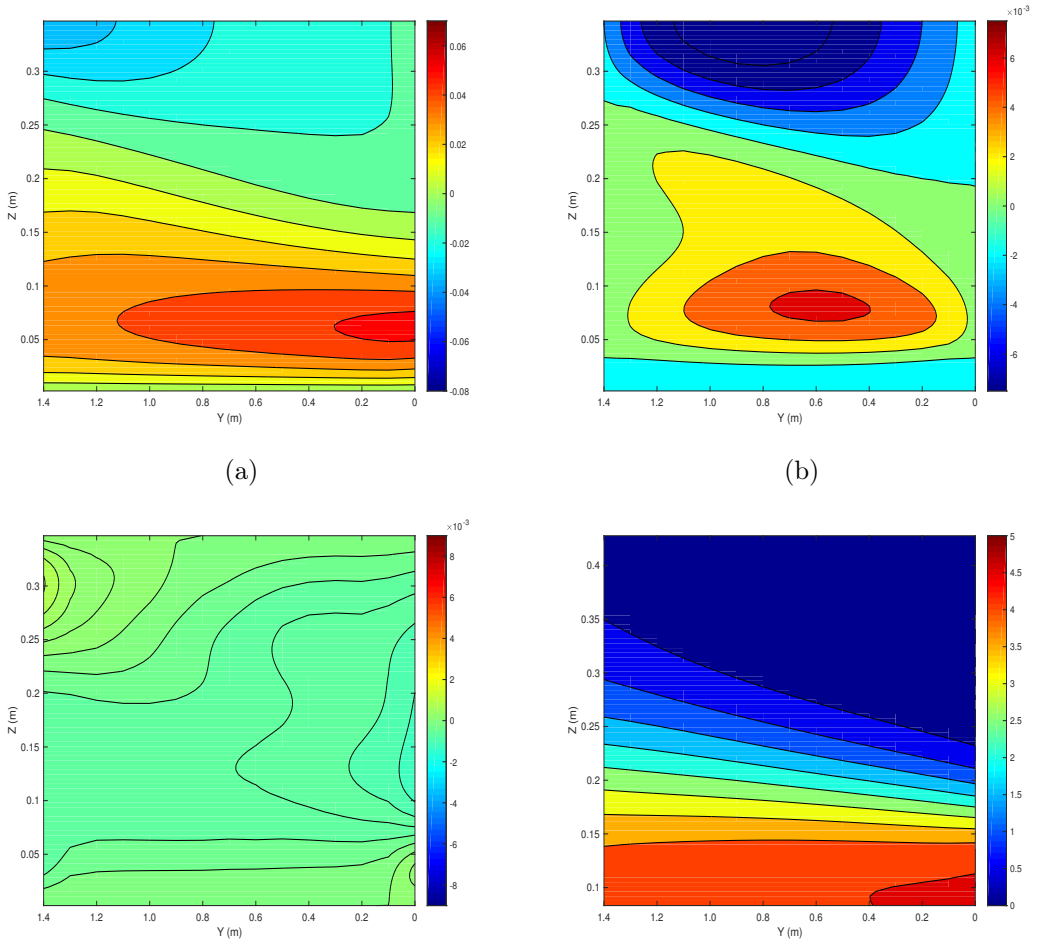

Figure 19: Across-channel results from the top of the sill after 500 seconds in the single-layered flow case with the Coriolis parameter $f = 0.0267$ s^{-1} (Experiment 10). (a) shows the horizontal velocity U in ms^{-1}, (b) shows the horizontal velocity V in ms^{-1}, (c) shows the vertical velocity W in ms^{-1} and (d) shows the density-distribution. The horizontal axes show the width Y in meters, and the vertical axes show the depth Z in meters.

With double the value of the Coriolis parameter, the dense and light water are nearly mixed all the way to the surface on the left side of the channel (Figure 20 (d)). The mixing on the right side is less, but still more than for the case with $f = 0.0267$ s^{-1}. This gives a steep slope in the denser layers. Because of the mixing, the most dense water seems to be pulled towards the acceleration at the lower right part of the channel, which also the reason why there is a slight sloping downwards on the left side of the channel in the second most dense layer.

The maximum horizontal velocity U is found on the lower right side of the channel and is at about $U = 0.05$ ms^{-1} (Figure 20 (a)). The positive velocity follows the slope in the density-distribution. In the whole upper part of the channel, the fluid has negative velocity, which is at its maximum in the upper left corner, at about $U = -0.04$ ms^{-1}. The combination between the large Coriolis parameter and the lowered height over the sill clearly creates the best conditions for the return flow to occupy more space of the channel, as it is in the largest area of all the experiments, however, it is not the fastest, as its velocity is as large as the ones in both experiments 3 and 10.

The maximum positive velocity, at $V = 0.01$ ms^{-1}, is found in the middle of the lower part of the channel, slightly towards the right side (Figure 20 (b)). The shape of this fluid mass has a more rounded shape than in the case of $f = 0.0267$ s^{-1}. Either it is located too far from the left wall or the vertical currents are wrong, such that the fluid does not get the figure eight shape. Results from the vertical velocity show that it could be a combination of both these factors (Figure 20 (c)). In the upper part of the channel, currents of negative rightwards velocity are located. With a maximum of about $V = -0.02$ ms^{-1}, it occupies most of the surface of the channel, located slightly leftward from the middle. Rotation is the most likely cause behind the shear in the two flows. The transverse circulation in this experiment is much stronger than in the case with the lower Coriolis parameter, indicating that the strength of the currents are highly affected by the choice of f.

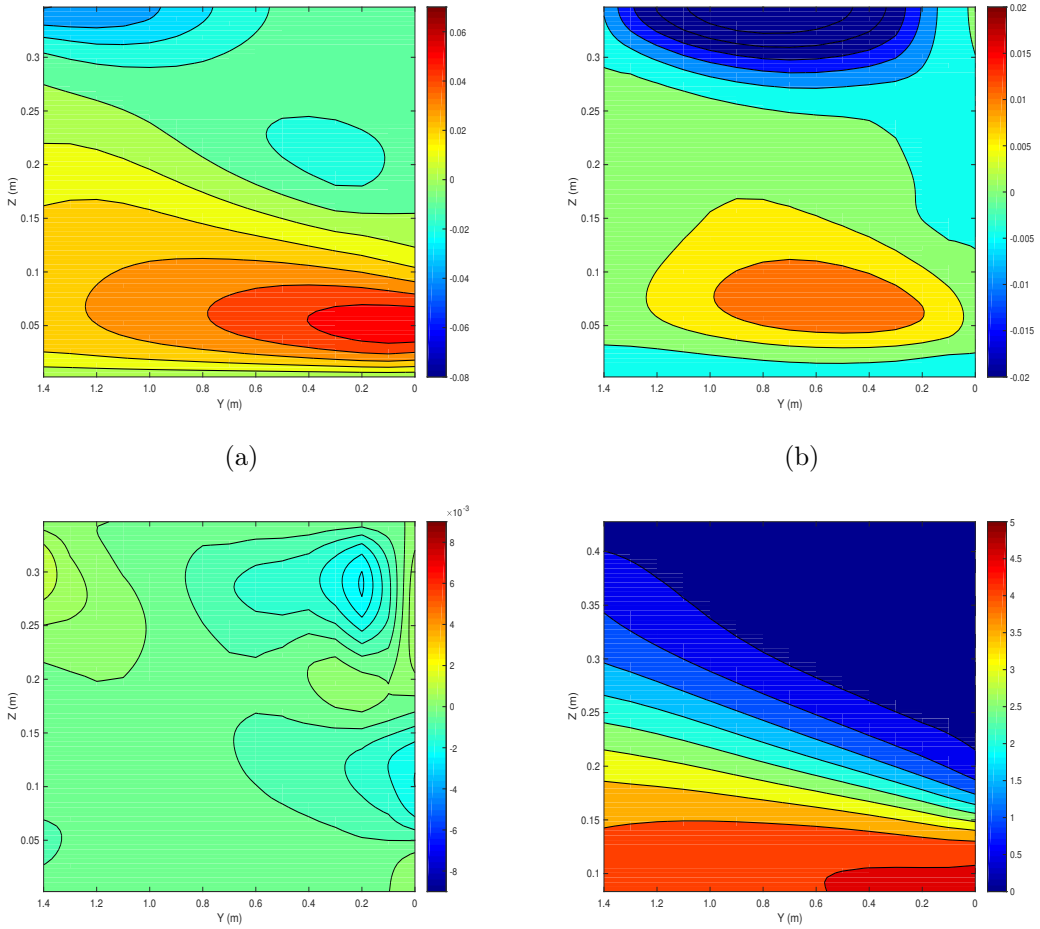

Figure 20: Across-channel results from the top of the sill after 500 seconds in the single-layered flow case with double the value of the Coriolis parameter, at $f = 0.0534$ s^{-1} (Experiment 11). (a) shows the horizontal velocity U in ms^{-1}, (b) shows the horizontal velocity V in ms^{-1}, (c) shows the vertical velocity W in ms^{-1} and (d) shows the density-distribution. The horizontal axes show the width Y in meters, while the vertical axes show the depth Z in meters.

When using half the value of the Coriolis parameter, there are still some mixing such that the dense water reaches high up in the channel, but the sloping in the density layers is less significant (Figure 21 (d)). The thickness of the pycnocline implies more mixing on the left side of the channel than on the right, caused by the rotation. The most dense water, at about $\rho = 1004.5$ kgm^{-3}, seems to be pulled towards the right lower corner, probably due to the enhanced mixing on the left side, which also could be the explanation for why there is a slight downwards bend in the second most dense layer at the left side wall.

The horizontal velocity U does not have a distinct maximum value on the lower right side of the channel. Instead the maximum velocity lies in a belt reaching all the way across the width, and it is at about $U = 0.04$ ms^{-1} (Figure 21 (a)). The velocity layer is more than twice as thick on the right side than on the left, indicating that the rotation still has an effect on the along-channel velocity. An assumption is that if more time is given, the water of maximum velocity will eventually let go of the left side wall and be concentrated on the right side. The lower Coriolis parameter may cause too little rotation for the flow to have been properly developed as it has in the two other cases with $f = 0.0267$ s^{-1} and $f = 0.0534$ s^{-1}. In the upper 0.1 m of the channel, there is a return flow, with maximum about $U = -0.02$ ms^{-1}, which is found at the left corner. This adds to the assumption that the rotation and the lowered water depth above the sill together contributes in letting the return flow occupy the whole width of the channel.

The transverse circulation cell is weaker than in the cases with more rotation. The maximum positive velocity, at about $V = 3 \times 10^{-3}$ ms^{-1}, is found in the middle of the lower part of the channel, located slightly rightwards (Figure 21 (b)). The area of water of positive velocity have the distinct figure eight shaped curves on the left side, implying that there are vertical currents from the flow reaching the wall and being forced either up or down (Figure 21 (c)). This could also be a factor that causes the slope in the density-distribution. In the upper part of the channel, the negative rightwards flow is located. The maximum velocity, at about $V = -5 \times 10^{-3}$ ms^{-1}, is found at the surface in the middle of the channel, slightly leftward. This shear of the velocities is caused by the rotation.

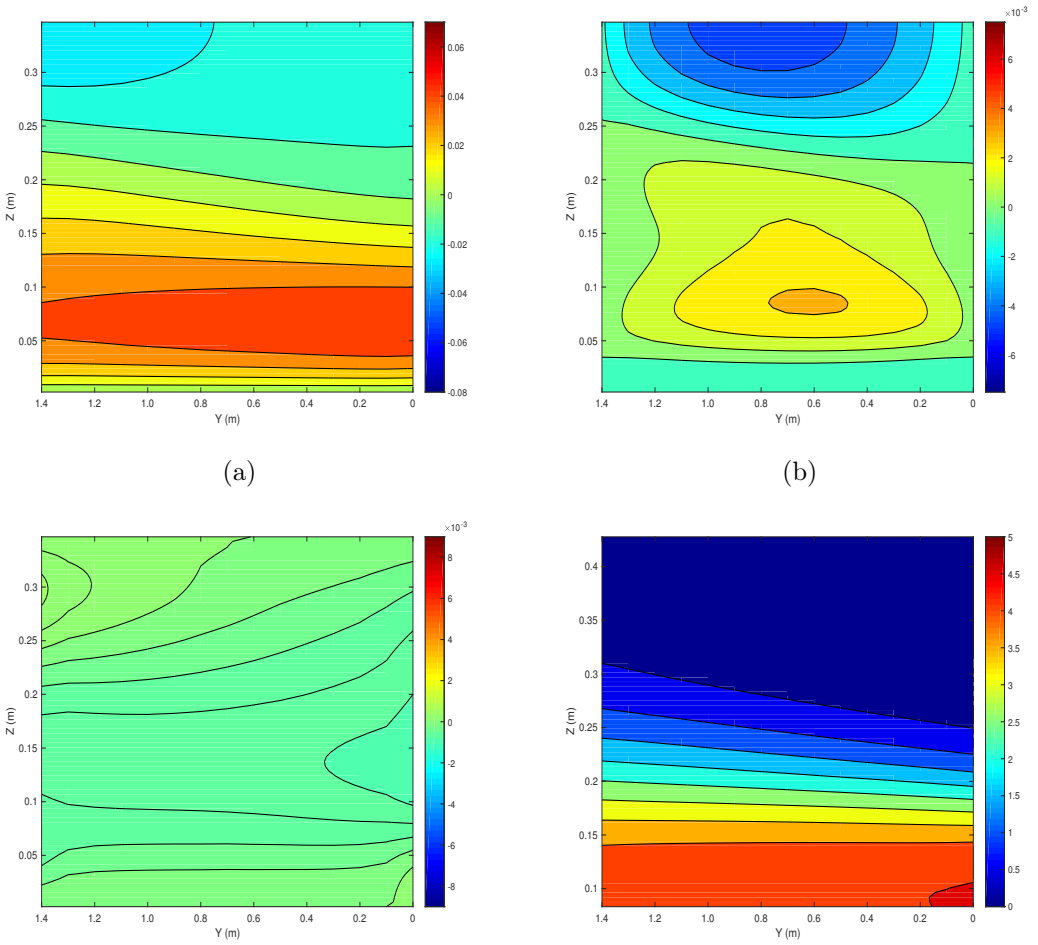

Figure 21: Across-channel results from the top of the sill after 500 seconds in the single-layered flow case, with half the value of the Coriolis parameter, at $f = 0.01335$ s^{-1} (Experiment 12). (a) shows the horizontal velocity U in ms^{-1}, (b) shows the horizontal velocity V in ms^{-1}, (c) shows the vertical velocity W in ms^{-1}, and (d) shows the density-distribution. The vertical axes show the depth Z in meters, and the horizontal axes show the width Y in meters.

4.3.2 Two-layered flow case

The upper flow together with the decreased sill depth creates a blocking of the saline lower flow, preventing it from passing over the sill (Figure 22). As the dense flow is about to climb over the edge of the sill, the lighter flow is released, forcing the dense flow to retreat into the outer basin M.

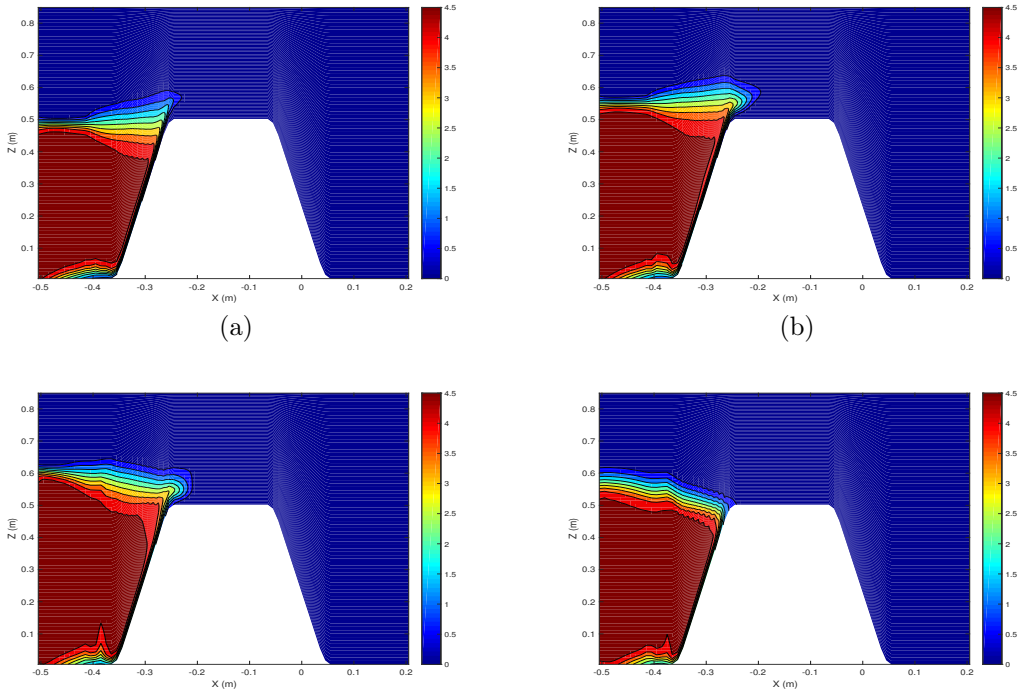

Figure 22: Along-channel results from the middle of the channel in the two-layered flow case (Experiment 14). They show the density-distribution after (a) 250 seconds, (b) 300 seconds, (c) 350 seconds and (d) 400 seconds. The vertical axes show the depth Z in meters, and the horizontal axes show the length X in meters.

Adding the rotation to this case showed little effect on the horizontal velocity U. All three cases of the Coriolis parameter have about the same velocities. The only difference is that there are a slight slope up on the left side and down on the right side, which is a little bit enhanced in the doubled Coriolis parameter case (Figure 23 (c)), and a little weaker in the halved Coriolis parameter case (Figure 23 (e)).

A transverse circulation cell occupying the whole width and depth of the cross-sectional area can be found in all three cases (Figure 23 (b), (d) and (f)). The only difference to be found is that the doubled Coriolis parameter gives a slightly stronger flow, while the halved Coriolis parameter gives a weaker flow. At $f = 0.0267$ s^{-1}, the maximum velocities towards left and right are $V = 3 \times 10^{-3}$ ms^{-1} and $V = -4 \times 10^{-3}$ ms^{-1}, respectively. In comparison, in the doubled Coriolis parameter case the maximum velocities are $V = 4 \times 10^{-3}$ ms^{-1} and $V = -8 \times 10^{-3}$ ms^{-1}, and in the halved Coriolis parameter case the maximum velocities are $V = 1 \times 10^{-3}$ ms^{-1} and $V = -2 \times 10^{-3}$ ms^{-1}.

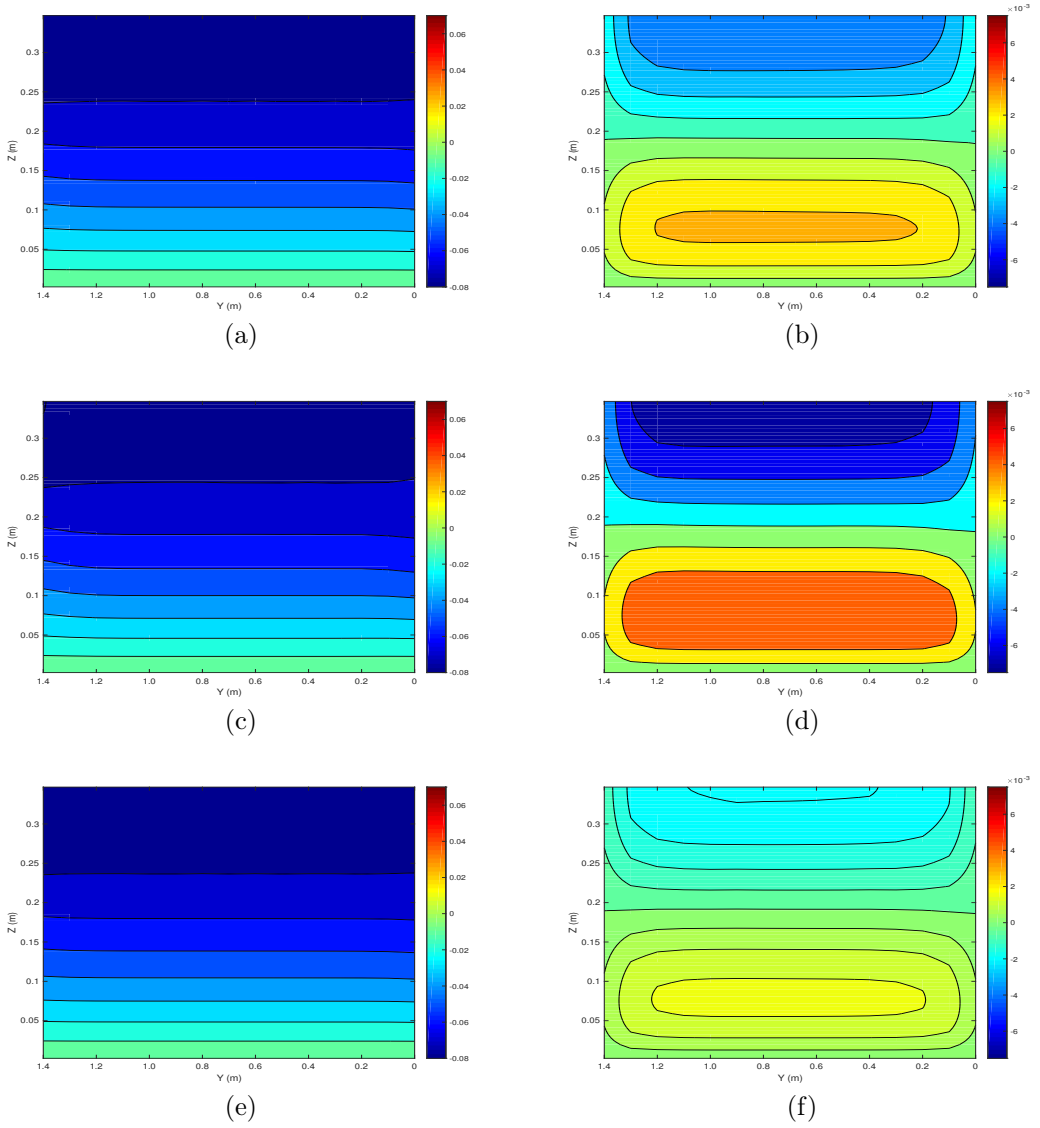

Figure 23: Across-channel results from the top of the sill after 500 seconds in the two-layered flow case. (a) shows the horizontal velocity U in ms^{-1} and (b) shows the horizontal velocity V in ms^{-1} when $f = 0.0267\ \mathrm{s}^{-1}$ (Experiment 14). (c) shows the horizontal velocity U in ms^{-1} and (d) shows the horizontal velocity V in ms^{-1} when $f = 0.0534\ \mathrm{s}^{-1}$ (Experiment 15). (e) shows the horizontal velocity U in ms^{-1} and (f) shows the horizontal velocity V in ms^{-1} when $f = 0.01335\ \mathrm{s}^{-1}$ (Experiment 16). The horizontal axes show length Y in meters, while the vertical axes show depth Z in meters.

5 Concluding remarks

A total of 16 experiments have been conducted in this thesis. The first eight with a density difference of $\Delta\rho = 5.1$ and a sill depth of $h_b = 0.43$ m. Two flow systems have been studied in particular, a single-layered flow case and a two-layered flow case. Rotational effects have been studied and compared to the flow without rotation, and the sensitivity to the choice of Coriolis parameter have been in focus. For experiments 9 to 16, the water depth was lowered, such that the sill depth was $h_b = 0.349$ m, and the density-difference was changed to $\Delta\rho = 4.7$. As in the first eight experiments, there are two main cases, a single-layered flow case and a two-layered flow case. Results are compared with and without rotation, using the same three values of the Coriolis parameter as previously. Before these experiments were run, a sensitivity study was done to chose appropriate mixing coefficients and number of vertical grid cells. The main goals have been to first find out if the numerical model could recreate the results from Cuthbertson et al. (2017), and then to study all the effects of adding rotation to the numerical model.

The most interesting feature of the added rotation, found in all the experiments, was a transverse circulation cell across the channel in the results from the horizontal velocity V. The cases with double the value of the Coriolis parameter generally had stronger currents in this circulation, with larger values than the rest by an order of magnitude. The experiments with the single-layered flow case, experiments 2 to 4 and 10 to 12, were correspondingly similar in the horizontal velocity V for the three rotational parameters. The only substantial difference was found in the negative velocity in experiment 10, which was more than three times as large as in the corresponding experiment 2. As it is in the order $O(10^{-3})$, this might not have much significance.

The positive horizontal velocities V in the experiments with the two-layered flow case, experiment 6 to 8, had a magnitude about twice the values of the corresponding single-layered flow case experiments 2 to 4. The negative horizontal values were about the same, except for with $f = 0.0267$ s^{-1}, where the two-layered flow case had a velocity at more than three times the magnitude than the single-layered flow case. The reason for this increased circulation must lay in the larger velocity shear between the two flows in opposite directions, as it leads to more mixing. When the water is more mixed, there is more movement across the channel as the water compensates for the change in the density. This could also mean that the shear force enters in the balance that previously has only been significantly between the Coriolis force and the pressure force.

In all experiments, except for in the single-layered flow case with $f = 0.0267$

s^{-1}, the circulation cell was slightly sheared, where the limit between them sloped down from the left side to the right, and the maximum positive velocity was located slightly towards the right side, while the maximum negative velocity was located slightly towards the left side. This is probably a result of the mixing and vertical advection moving water up on the left side of the channel. The shift can also be somewhat explained by the positive lower current reaching the left side wall and being forced upwards, and the negative upper current reaching the right side wall being forced downwards, and by this transporting water up and down, respectively. In the two-layered flow case with double the value of the Coriolis parameter, both the maximum velocity areas were located towards the left side, probably because of a combination between the stronger rotation and the shear velocities in opposite directions.

Because of vertical flow along the left side wall, the water of positive velocity got a figure eight shaped curve on the left side. The current that reaches the wall divides into an upwards flow and a downwards flow, which creates the characteristic curve.

The rotation created a velocity variation across the channel, and in the experiments with the single-layered flow case, the maximum velocity was located at the lower right side. In experiment 12, with half the value of the Coriolis parameter, the maximum velocity was found in a belt along the whole width of the channel, but as this belt was three times as thick on the right side as on the left, the same assumptions as in the other single-layered flow cases applies.

For the experiments with the two-layered flow case, the maximum horizontal velocity U was located more towards the left side, in the middle of the channel for the experiments 6 and 7, and all the way towards the left side wall in experiment 8. The outcome is that the forces from the upper flow, or the shear between the flows, balances out the effect of the rotation yielding that the water is accelerated the most towards the right side of the channel. Another explanation could be that the open boundary at the bottom of the inner basin I does not remove the appropriate amount of water. The water flowing into this basin has higher velocity than the water coming in at the outer basin M and a higher volume transport due to mixing along the way. This can result in a pile up of dense water in the inner basin, creating a pressure gradient towards the outer basin M. As the pressure increases, this can balance out the force of the water of highest velocity, and the maximum velocity then seems to have moved leftwards across the channel.

All experiments, except for experiments 14 to 16, had density-distribution indicating more mixing on the left side than on the right. Dense water was mixed higher up on the left side, which led to a slope in the results, visible in both the density-distribution and the horizontal velocity U. The magnitude of the slope apparently

depended on the value of the Coriolis parameter, as there seemed to be more mixing in the cases with more rotation. This was not a consequent feature, as other factors also were important for the mixing.

As documented in the single-layered flow case with $f = 0.0267$ s^{-1}, the plume was higher on the left side of the channel than on the right side. Even if the along-channel current speed was higher on the right side than the left, the slope in the dense water causes the plume to reach the sill on the left side before it can climb up to this height in the channel on the right. Naturally, the flow also reaches the inner basin on the left side before the right side.

In the two-layered flow case with double the value of the rotation parameter, the dense flow was outcropped by the light flow Q_1. The rotation was so strong that it managed to pull all the dense water towards the left side of the channel.

The experiments with the single-layered flow case with double the value and half the value of the Coriolis parameter, and the experiments 10 to 12, had a return flow in the upper part of the channel. This was expected to be a result of the boundary condition at the wall in the inner basin I not being able to take out enough water of the channel, which led to a flow being sent back into the channel again.

In experiments 14 to 16 with the two-layered flow case, all had a transverse circulation cell across the width of the channel. The rotation cell occupied the whole channel in all three cases, with positive velocity in the lower half and negative velocity in the upper half. Although the experiments were classified from strong to weak, with the largest Coriolis parameter to the lowest, the range for the horizontal velocity was only between $V = 4 \times 10^{-3}$ ms^{-1} and $V = -8 \times 10^{-3}$ ms^{-1}. The tendency is therefore the same, but the differences are modest.

If bends and curves were present in the channel in this thesis, the centrifugal force would be expected to have a more central role in the dynamics of this experiment. As it is now, there is no significant contribution from the centrifugal force, and it is therefore excluded from the governing equations.

These results will have relevance for at least some Norwegian fjords. They typically have layered water masses at the coast outside, and relatively narrow sills at the entrance preventing horizontal water exchange between the coastal ocean and the fjord basins. If dense water is entering the sill area at a height suitable for overflow, this will be an analogue to the single-layered flow case in this thesis. For narrow fjords, i.e. width much less than the internal radius of deformation (or the internal Rossby radius), which typically have a value of $\sim$5 km in Norway, the results without rotation will apply. More realistic though, are the results of the rotating cases. This will be relevant for many fjords in Norway, and the second order circulation cell in the across-channel plane will most likely be present. To find empirical evidence of

this, in a situation with many other simultaneous current components like the tide, is hard, and that may be the reason for the lack of previous reports in the literature.

If the sill is much shallower, maybe only $10 - 20$ m, the two-layered flow case may be relevant. The surface outflow can be the estuarine circulation in the brackish layer or outflow in an Ekman layer due to wind. A simultaneous upwelling favorable wind at the coast can lift the dense water outside the sill area and a dense overflow might occur. Similarly as for the single-layered flow case, rotation will produce a second order clockwise circulation cell.

For both cases, this second-order circulation will result in somewhat enhanced mixing of the water and create vertical advection. The magnitude will probably not be very large, since previously not reported.

It can be questioned if the set up of the numerical simulation, mimicking a small laboratory tank and with very high grid resolution, is relevant for a natural situation. Also, the artificial open boundary condition at each end of the channel might put unrealistic limitations on the results. Nevertheless, the recreation of the measurements of the laboratory experiments gives confidence that the results contain some credibility.

A next step could be to reproduce the numerical simulation using geophysical scales and a natural value of the Coriolis parameter. Also, the inclusion of other current components, like the tide, might be of interest to see if this inhibits mechanisms responsible for the found second order transverse circulation.

6 Acknowledgements

I would like to use this opportunity to thank my supervisor, Jarle Berntsen, for strict, but fair guidance, interesting discussions around the topic and helpful comments throughout the work of this thesis.

I would also like to thank my father for being my unofficial supervisor and help me every time I have had a question about interpretation, phrasing or other important factors. The rest of my family and friends should also have a big thanks for all the support and encouragement they have shared with me. I love you all!

Many thanks to professor Benoit Cushman-Roisin for a brief but very interesting discussion at the end of my work with this thesis. I wish I had reached out to you earlier.

And last, but not least, I would like to thank my boyfriend for the great and loving support, and for enduring all my ups and downs the last couple of years. I could not have done this without you!

7 References

1. Asplin, L., Vea Salvanes, A. G. and Kristoffersen, J. B. (1999). *Nonlocal wind-driven fjord-coast advection and its potential effect on plankton and fish recruitment.* Fish. Oceanogr. 8:4, pp. 255-263.

2. Avlesen, H. and Berntsen, J. (2001). *Flow over rough topography. A preliminary study with high resolution topography at Ormen Lange.* Technical report No. 209, The Nansen Environmental and Remote Sensing Center

3. Berntsen, J. (2000). *Users guide for a modesplit σ-coordinate numerical ocean model.* Tech. Rep. 135, Dept. of Applied Mathematics, University of Bergen, Johs. Bruns gt. 12, N-5008 Bergen, Norway, 48 p.

4. Berntsen, J., Aksnes, D. L. and Foldvik, A. (2002). *Production enhancement by artificial upwelling: A simulation study.* Hydrobiologica 484, pp. 177-190.

5. Berntsen, J., Alendal, G., Avlesen, H. and Thiem, Ø. (2018). *Effects of the bottom boundary condition in numerical investigations of dense water cascading on a slope.*

6. Berntsen, J., Darelius, E. and Avlesen, H. (2016). *Gravity currents down canyons: Effects of rotation.* Ocean Dyn. 66, pp. 1353-1378.

7. Cushman-Roisin, B. and Beckers, J.-M. (2011). *Introduction to Geophysical Fluid Dynamics.* Academic Press Inc, p. 875.

8. Cuthbertson, A., Laanearu, J., Carr, M., Sommeria, J. and Viboud, S. (2017). *Blockage of saline intrusions in restricted, two-layer exchange flows across a submerged sill obstruction.* Environ Fluid Mach, Vol. 18, Issue 1, pp. 27-57.

9. Darelius, E. (2008). *Topographic steering of dense overflows: Laboratory experiments with V-shaped ridges and canyons.* Deep-Sea Research I 55, pp. 1021-1034.

10. Farmer, D. M. and Freeland, H. J. (1983). *The physical Oceanography of Fjords.* Prog. Oceanog. Vol. 12, pp. 147-220.

11. Davies, P. A., Wåhlin, A. K. and Guo, Y. (2005). *Laboratory and Analytical Model Studies of the Faroe Bank Channel Deep-Water Outflow.* Journal of Physical Oceanography, Vol. 36, pp. 1348-1364.

12. Freeland, H. J. and Farmer, D. M. (1980). *Circulation and energetics of a deep, strongly stratified inlet.* Can. J. Fish. and Aquatic Sci., 37(9), pp. 1398-1410.

13. Gade, H. G. and Edwards, A. (1980). *Deep water renewal in fjords.* Fjord Oceanography (1980).

14. Keilegavlen, E. and Berntsen, J. (2009). *Non-hydrostatic pressure in σ-coordinate ocean models.* Ocean Modelling 28, pp. 240-249.

15. Martinsen, E. A. and Engedahl, H. (1987). *Implementation and testing of a lateral boundary scheme as an open boundary condition for a barotropic model.* Coastal Eng., 11, pp. 603-637.

16. Mellor, G. L. and Yamada, T. (1982). *Development of a Turbulence Closure Model for Geophysical Fluid Problems.* Reviews of geophysics and space physics, Vol. 20, No. 4, pp. 851-875.

17. Pedlosky, J. (1982). *Geophysical fluid dynamics.* Springer-Verlag, New York, 604 p.

18. Prastowo, T., Griffiths, R. W., Hugher, G. O. and Hogg, A. McC. (2008). *Mixing efficiency in controlled exchange flows.* J. Fluid Mech., Vol. 600, pp. 235-244.

19. Pratt, L. J. (2004). *Recent progress on understanding the effects of rotation in models of sea straits.* Deep-Sea Research II 51, pp. 351-369.

20. Stigebrandt, A. (1980). *Some aspects of tidal interaction with fjord constrictions.* Estuarine, Coastal and Shelf Science, 11, pp. 151-166.

21. Stigebrandt, A. (1981). *A Mechanism Governing the Estuarine Circulation in Deep, Strongly Stratified Fjords.* Estuarine, Coastal and Shelf Science I3, pp. 197-211.

22. Stigebrandt, A. (2012). *Hydrodynamics and circulation of fjords.* In: Bengtsson L, Herschy RW, Fairbridge RW, editors. Encyclo-pedia of Lakes and Reservoirs, Berlin: Springer, pp. 327-344.

23. Stigebrandt, A. and Aure, J. (1989). *Vertical Mixing in Basin Waters of Fjords.* American Meteorological Society, Vol. 19, pp. 917-926.

24. Umlauf, L. and Arneborg, L. (2009). *Dynamics of Rotating Shallow Gravity Currents Passing through a Channel. Part I: Observations of Transverse Structure.* Journal of Physical Oceanography, Vol. 39, pp. 2385-2401.

25. Umlauf, L. and Arneborg, L. (2009). *Dynamics of Rotating Shallow Gravity Currents Passing through a Channel. Part II: Analysis.* Journal of Physical Oceanography, Vol. 39, pp. 2401-2416.

26. Umlauf, L., Arneborg, L., Hofmeister, R. and Burchard, H. (2010). *Entrainment in Shallow Rotating Gravity Currents: A modeling study.* Journal of Physical Oceanography, Vol. 40, pp. 1819-1834.

27. Whitehead, J. A. (1998). *Topographic control of oceanic flows in deep passages and straits.* Reviews of Geophysics, 36, pp- 423-440.